

Tephrostratigraphy of proximal pyroclastic sequences at Mount Melbourne (northern Victoria Land, Antarctica): insights into the volcanic activity since the last glacial period.

P. Del Carlo¹, A. Di Roberto^{1*}, G. Di Vincenzo², G. Re¹, P.G. Albert³, M. Nazzari⁴, V.C. Smith⁵, A. Cannata^{6,7}.

(1) *Istituto Nazionale di Geofisica e Vulcanologia, Sezione di Pisa, via C. Battisti 53, 56125 Pisa, Italy*

(2) *Istituto di Geoscienze e Georisorse, Consiglio Nazionale delle Ricerche, (IGG-CNR), Via G. Moruzzi 1, 56124, Pisa, Italy*

(3) *Department of Geography, Swansea University, Singleton Park, Swansea, SA2 8PP, UK*

(4) *Istituto Nazionale di Geofisica e Vulcanologia, Sezione di Roma1, via di Vigna Murata 605, 00143, Roma, Italy*

(5) *Research Laboratory for Archaeology and the History of Art, School of Archaeology, University of Oxford, 1 South Parks Road, OX1 3TG, UK*

(6) *Dipartimento di Scienze Biologiche, Geologiche e Ambientali, Università di Catania, Corso Italia 57, 95125 Catania, Italy*

(7) *Istituto Nazionale di Geofisica e Vulcanologia, Osservatorio Etneo, Piazza Roma 2, 95125 Catania, Italy*

*Corresponding author Alessio Di Roberto: alessio.diroberto@ingv.it

Keywords: Antarctica, Mount Melbourne, Explosive eruptions, Tephra, Glass geochemistry, ⁴⁰Ar-³⁹Ar dating

Abstract

We report on the characterization of a thick sequence of pyroclastic deposits exposed on the summit area and flanks of Mount Melbourne volcano, in northern Victoria Land,

Antarctica related to eruptions during the Late Glacial period. We provide a complete characterization of tephra deposits including mineralogy, single shard major- and trace-element glass compositions, and an ^{40}Ar - ^{39}Ar age of feldspar crystals extracted from the deposit. The pyroclastic deposits are trachybasaltic to trachytic in composition and are interpreted to have resulted from four Strombolian/Vulcanian to sub-Plinian/Plinian eruptions. The younger and more intense sub-Plinian/Plinian eruption (our *eruption 2*) yielded an ^{40}Ar - ^{39}Ar age of 13.5 ± 4.3 ka ($\pm 2\sigma$). The study of Mount Melbourne proximal deposits provides significant new data for the reconstruction of the volcano eruptive history and a better assessment of the volcanic risk connected to a possible future eruption.

We also explore geochemical correlations between Mount Melbourne proximal deposits and distal tephra layers recognized in ice cores and blue ice fields of East Antarctica. A good geochemical match exists between the composition of products from the trachytic sub-Plinian/Plinian *eruption 2* and some tephra layers from Talos Dome and shards in Siple Dome which is also compatible in age (c. 9.3 ka) with our ^{40}Ar - ^{39}Ar age determination. Our new insights into the volcanic history of Mount Melbourne and the new high-quality electron microprobe and trace element composition data on its proximal products will help improve future correlations and synchronization of tephra archives in the region.

1. Introduction

Recent years have seen significant advances in our knowledge and understanding of Antarctic volcanism owing to the extensive research carried out during the seasonal presence of scientists and technicians on the continent. Geological surveys, and the installation and significant improvements to the ground-based monitoring networks at some of the active volcanoes are providing new data on the eruptive history of Antarctic volcanoes and their current status (Gambino et al., 2021; Geyer et al., 2021; Sims et al., 2021). In particular, the study of tephra (volcanic ash) layers produced by explosive eruptions of Antarctic volcanoes have provided relevant information about

57 source volcanoes and volcanic systems including the age of the eruptions, and the style
58 and intensity of the volcanic activity (Del Carlo et al., 2015; Di Roberto et al., 2019;
59 2020; 2021a; Iverson et al., 2014; Lee and Lee, 2017; Lee et al., 2019; Narcisi et al.,
60 2010; Narcisi and Petite, 2021 and references therein). In Antarctica, as in many other
61 geographical contexts, tephra deposits are proving invaluable in paleoenvironmental
62 and paleoclimate studies since they represented a powerful chrono-stratigraphical tool
63 that can be used to date sedimentary archives, enable their correlation over significant
64 distances, and link and synchronize different types of records (outcrops, marine
65 sediments and ice cores; Di Roberto et al., 2021b).

66 In addition, the presence of permanent scientific bases in the vicinity of some of the
67 Antarctic volcanoes (for example the Argentine and Spanish bases on Deception
68 Island) and the rapidly growing tourism in the Antarctic region make it crucial to
69 increase our knowledge of the eruptive history of these volcanoes, in order to define
70 the potential hazards associated with future eruptions (Geyer et al., 2021). Mount
71 Melbourne is one of the largest active volcanoes of Antarctica and the last eruption is
72 thought to have occurred around 1892 CE (Geyer, 2021 and references therein). The
73 Mario Zucchelli Station (Italian), Jang Bogo (Korea), Gondwana (Germany) bases and
74 the new China station are located between 65 and 30 km from the summit of Mount
75 Melbourne and are within the range of significant ash fallout in the case of an intense
76 explosive eruption. In the second half of the 1980s, the Italian National Antarctic
77 Research Program (PNRA) began numerous activities in northern Victoria Land, some
78 of which were focused on investigating and monitoring Mount Melbourne volcano. In
79 particular, a global positioning system (GPS), tilt and seismic networks were installed
80 on the volcano summit and flanks, and a volcanological observatory was set up in 1988
81 (Bonaccorso et al., 1997). From 2016, new seismological, geochemical and
82 volcanological research was carried out on Mount Melbourne in the framework of the
83 ICE-VOLC Project. A review of the volcanological investigations and monitoring
84 results achieved over the last 30 years for Mount Melbourne has been recently
85 published by Gambino et al. (2021). In particular, these authors report that the volcano

shows signs of activity including the magmatic signature of geochemical fluids from active fumaroles, seismicity comprising both long-period events and tremor and ground deformation with evidence of slow inflation/deflation around the summit area. Further signs of relatively recent activity of Mount Melbourne include tephra exposures in the summit and flanks of the volcano (see Giordano et al., 2012 and references therein), which are thick and suggest that intense explosive eruptions occurred in the recent past. Mount Melbourne should be considered capable of producing large eruptions ($VEI > 3$) with high eruptive plumes, with the potential for transcontinental ash dispersal that could result in significant consequences to global aviation safety (Geyer et al., 2017). Consequently, it is critical to correctly assess the nature, dynamics, intensity, and recurrence interval of Mount Melbourne eruptions to evaluate the future potential volcanic hazard.

With this aim, a complete characterization of proximal deposits from high explosive eruptions of Mount Melbourne is of great importance. In this paper, we provide a volcanological reconstruction of activity that deposited the uppermost pyroclastic sequence of Mount Melbourne. We present geological data from field observations of the pyroclastic deposits exposed in the summit area and on the flank of the volcano, which were made during the XXXII Italian Antarctic Expedition (2016-2017) in the framework of the ICE-VOLC project (PNRA). We also sampled the units and provide the tephra characterization including mineralogy, major- and trace-element glass compositions, and ^{40}Ar - ^{39}Ar data obtained on feldspar crystals extracted from a trachytic pumice deposit. Based on these data, we make inferences on the last cycle of eruptions from Mount Melbourne.

These new data are also useful for tephrochronological studies and in particular, for the precise identification of Mount Melbourne derived tephra layers. These tephra layers can now be used to assess reliable proximal-distal correlations and for the dating, correlation and synchronization of paleoclimate archives in the region.

2. Geological background

115 Northern Victoria Land is part of the McMurdo Volcanic Group, one of the largest
116 areas of Cenozoic volcanic rocks in Antarctica. The northern Victoria Land hosts a
117 very long record of rift-related igneous activity including plutonic rocks and cogenetic
118 dyke swarms spanning from about 50 to 20 Ma. The volcanism in northern Victoria
119 Land started in the middle Miocene (c. 15 Ma) with activity largely concentrated
120 between the Late Miocene (<10 Ma) and the present (Smellie and Rocchi, 2021). The
121 origin of the entire igneous suite was long debated but presently the most accepted
122 model sees no role for a mantle plume (Rocchi and Smellie, 2021). According to this
123 model, the growth of the largest volcanic edifices along the Ross Sea coast since the
124 middle Miocene was governed by lithospheric necking. Conversely smaller central
125 volcanoes and scoria cones located inland would result from the establishment of
126 magma chambers in the thicker crust (Rocchi and Smellie, 2021). Volcanoes of the
127 northern Victoria Land include quite large multiple coalesced shield volcanoes,
128 relatively small stratovolcanoes, and tiny monogenetic volcanic centres with scoria
129 cones that belong to two main volcanic provinces, the Hallett and Melbourne volcanic
130 provinces (Smellie and Rocchi, 2021). In the Melbourne volcanic province, Mount
131 Melbourne and Mount Rittmann volcanoes have been active in recent times as a large
132 number of Late Pleistocene to Holocene tephra layers found in the glacial and marine
133 archives have been correlated to these sources (Del Carlo et al. 2015; Di Roberto et al.
134 2019; Dunbar et al. 2003; Narcisi et al. 2010). Mount Melbourne is located between
135 Wood Bay and Terra Nova Bay and is now quiescent (Figs. 1 and 2). The volcano has
136 a basal diameter of c. 21-24 km and a maximum elevation of 2732 m. The edifice is
137 largely covered by snow and ice, except for the summit region and sparse rock
138 exposures on the east side that extend down to c. 1800 m in elevation. The volcano
139 shows a gentle conical shape, with undissected flanks, apart from a small scar located
140 on the eastern side that is possibly linked to a landslide event (Giordano et al., 2012),
141 and has a well-formed ice-filled crater c. 700 m in diameter that has also been
142 interpreted as a summit caldera (Armienti et al., 1991).

143 A comprehensive synthesis of Mount Melbourne volcanic evolution is presented in
144 Wörner and Viereck (1990) and Giordano et al. (2012), which is based on stratigraphic
145 and geochemical data and ^{40}Ar - ^{39}Ar geochronology. The eruptive activity in the area
146 appears to have started with the formation of several monogenetic scoria cones and
147 lava flows over a wide area across the Transantarctic Mountains during the Lower
148 Pleistocene (Random Hills Period), which were mainly fed by alkali basaltic to
149 hawaiitic magmas. Afterwards, the volcanic activity became concentrated in the area
150 of the present-day Mount Melbourne stratovolcano, where deposits of several
151 monogenetic vents show the transition from subglacial/subaqueous to subaerial activity
152 during the Middle Pleistocene (Shield Nunatak Period). The early activity of the Mount
153 Melbourne stratovolcano is characterized by a trachytic ignimbrite that is dated at
154 123.6 ± 6.0 ka (Giordano et al. 2012) and indicates the formation of a crustal magma
155 system (Mount Melbourne Period). Following the ignimbrite, a succession of alkali
156 basaltic, hawaiitic, and subordinate benmoreitic lavas and scoria cones, dated at
157 90.7 ± 19.0 ka, were emplaced. The most recent deposit exposed at the top of Mount
158 Melbourne is mainly trachytic to rarely rhyolitic pumice fall deposits, probably
159 produced by a Plinian eruption (Giordano et al., 2012).

160 Presently, there is an extensive fumarolic and geothermal activity in the crater and on
161 the flanks of the volcano. The fumaroles have also produced several ice towers and a
162 complex network of ice caves near the summit area (Gambino et al., 2021; Lyon and
163 Giggenbach, 1974; Lyon, 1986; Wörner and Viereck, 1990)

164 The age of the last eruption from Mount Melbourne is still uncertain and there have
165 been no direct observations. Tephra layers have been found in glacier ice at several
166 places on the flanks of Mount Melbourne, suggesting that explosive activity may have
167 occurred in recent times. Lyon (1986) carried out the stable isotope analysis of two
168 snow profiles, at ca. 2000 m on the flanks of Mount Melbourne and the Campbell
169 Glacier, and estimated a snow accumulation rate of 0.5 and 2.2 m/a, respectively. Using
170 this accumulation rate, Lyon (1986) derived an age between 1862 and 1922 CE for the

uppermost ash layer that was found in an ice cliff on the western slope of Mount Melbourne.

Tephra layers have been also mapped on the eastern flanks of Mount Melbourne by Lee and Lee (2017) and Lee et al. (2019). These are grey, m-thick composed of pumice and crystals and yellowish-grey trachytic, pumice lapilli up to 20 cm-in diameter, embedded in ice. Based on the correlation between these proximal deposits and ash layers found in the Talos Dome ice core, Lee et al. (2020a, b) suggest there have been three Holocene eruptions from Mount Melbourne. The major element glass compositions of Talos Dome tephra layer TD85, dated at 670 ± 7 a BP (Narcisi et al., 2012; Severi et al., 2012), is thought to represent a Mount Melbourne eruption with the same age (the second one in stratigraphic order found by Lee and Lee (2017) and Lee et al. (2019) on Mount Melbourne proximal sites).

3. Materials and methods

In the austral summer of 2016-17, during the XXXII Italian Antarctic Expedition, we measured, described, and sampled the uppermost pyroclastic sequence exposed in the summit area and along the northern-western flank of Mount Melbourne volcano (Figs. 1, 3 and 4).

The samples were mounted in epoxy resin, sectioned and polished for the textural and geochemical analyses at the Istituto Nazionale di Geofisica e Vulcanologia, Sezione di Pisa (INGV-Pisa). A scanning electron microscope (SEM) was used to describe textures, and an Oxford Si(Li) energy-dispersive X-ray detector (EDS) was also used to determine mineral phase compositions. Major and minor element glass compositions of samples were determined using a JEOL 8600 wavelength-dispersive electron microprobe equipped with four spectrometers at the Research Laboratory for Archaeology and the History of Art, University of Oxford (operating conditions: 15 kV accelerating voltage, 6 nA beam current and a beam diameter of either 10 or 5 μm depending on the glass surface areas). The JEOL 8600 electron microprobe was calibrated with a suite of appropriate mineral standards; peak count times were 30 s for

all elements except Mn (40s), Na (12s), Cl (50s), P (60s). The PAP absorption correction method was used for quantification. Reference glasses from the Max Planck Institute (MPI-DING suite; Jochum et al., 2005) bracketing the possible chemistries were also analysed. These included felsic [ATHO-G (rhyolite)], through intermediate [StHs6/80-G (andesite)] to mafic [GOR132-G (komatiite)] glasses. All glass data have been normalised to 100% for comparative purposes. Uncertainties are typically $< \pm 0.8\%$ Relative Standard Deviation (RSD) for Si and $\sim \pm 5\%$ for most other major elements, except for the low abundance elements for instance Ti ($\sim \pm 7\%$) and Mn ($\sim \pm 30\%$). Additional analyses were conducted at the HPHT Laboratory INGV-Roma using a JEOL JXA 8200 electron microprobe equipped with five wavelength-dispersive spectrometers (operating conditions: 15 kV accelerating voltage, 8 nA beam current, 5 μm probe diameter, 10 and 5 s acquisition time for peak and background, respectively). For JEOL JXA 8200 EMPA the following standards were used: orthoclase (Si, Al, K and Na), apatite (F, P and Ca), forsterite (Mg), pyrite (Fe), rutile (Ti), tugtupite (Cl), and rhodonite (Mn). Sodium and potassium were analyzed first to prevent alkali migration effects. The precision of the microprobe was measured through the analysis of well-characterized synthetic oxide and mineral secondary standards. Based on counting statistics, analytical uncertainties relative to their reported concentrations indicate that for major elements precision was better than 5%. Analytical totals < 93 wt.% were discarded. Error bars on plots represent reproducibility, calculated as 2SD (standard deviation) of replicate analyses of MPI-DING StHs6/80-G.

The full glass dataset and the standard data are reported in Supplementary Table 1. Trace element analysis of volcanic glass was performed using an Agilent 8900 triple quadrupole ICP-MS (ICP QQQ) coupled to a Resonetics 193 nm ArF excimer laser-ablation in the Department of Earth Sciences, Royal Holloway, University of London. Full analytical procedures used are reported in Tomlinson et al. (2010). Spot sizes 20 and 25 μm were used depending on the vesicularity, crystal content, and ultimately the size of available glass surfaces. The repetition rate was 5 Hz, with a count time of 40 s on the sample, and 40 s on the gas blank to allow the subtraction of the background

229 signal. Blocks of eight or nine glass shards and one MPI-DING reference glass were
 230 bracketed by the NIST612 glass calibration standard (GeoREM 11/2006). In addition,
 231 MPI-DING reference glasses were used to monitor analytical accuracy (Jochum et al.,
 232 2005). The internal standard applied was ^{29}Si (determined by the EPM analysis). LA-
 233 ICP-MS data reduction was performed in Microsoft Excel. Accuracies of LA-ICP-MS
 234 analyses of MPI-DING glass standards ATHO-G and StHs6/80-G were typically <5%.
 235 Full glass datasets and MPI-DING standard glass analyses are provided in
 236 Supplemental Material 1.

237 ^{40}Ar - ^{39}Ar analyses were completed on a feldspar separate (grain size 0.25-0.50 mm),
 238 which was extracted from pumice lapilli through standard separation techniques,
 239 followed by handpicking under a stereomicroscope (sample MELS1-3). ^{40}Ar - ^{39}Ar
 240 analyses were determined through the laser step-heating technique at IGG-CNR (Pisa,
 241 Italy). The separate was leached in an ultrasonic bath at room temperature for a few
 242 minutes in diluted HF (7%) and was then wrapped in aluminium foil and irradiated in
 243 two distinct batches along with either the flux monitor Fish Canyon Tuff sanidine
 244 (irradiation PAV-80 lasting 5 hours) or the Alder Creek sanidine (irradiation PAV-82,
 245 lasting 2 hours). Irradiation for both batches was completed in the core of the TRIGA
 246 reactor at the University of Pavia (Italy). Argon isotope compositions for irradiation
 247 PAV-80 were acquired by a MAP215–50 single-collector noble gas mass spectrometer,
 248 fitted with a secondary electron multiplier. Gas purification (13 min, including ~3 min
 249 of lasering) was achieved by two SAES AP10 getters held at 400 °C, one SAES C-50
 250 getter held at room temperature and a liquid nitrogen cold trap. Blanks were analyzed
 251 every three to four analyses. A polynomial function was fit to blanks analyzed during
 252 the day of acquisition, and unknown analyses were corrected based on the time of
 253 measurement. Blanks are listed in Supplementary Table 2. Argon isotope compositions
 254 for irradiation PAV-82 were acquired by an ARGUS VI (Thermo Fisher Scientific)
 255 multi-collector noble gas mass spectrometer. Ar isotopes from 40 to 37 were acquired
 256 using Faraday detectors, equipped with $10^{12} \Omega$ resistors for ^{40}Ar and ^{38}Ar and $10^{13} \Omega$
 257 resistors for ^{39}Ar and ^{37}Ar . Faraday detectors were cross calibrated for the slight offset

258 using air shots. ^{36}Ar intensities were acquired by a Compact Discrete Dynode (CDD)
259 detector. The CDD is calibrated daily for its yield by measuring four to six air pipettes
260 prior to the first analysis. Gas purification (4 min, including ~3 min of lasering) was
261 achieved using three SAES NP10 getters (one water-cooled, held at ~400 C and two at
262 room temperature). Blanks were monitored every two runs and were subtracted from
263 succeeding sample results (Supplementary Material 2). More details about mass
264 spectrometer calibration and analysis can be found in Di Vincenzo et al. (2021). Mass
265 discrimination for both measurements acquired through the MAP215-15 and the
266 ARGUS VI mass spectrometers was determined before and after sample measurements
267 based on automated analyses of air pipettes (Supplementary Table 2). About 50 mg of
268 the feldspar separate from irradiation PAV-80 was spread onto the bottom of a 9-mm
269 hole of a copper holder, loaded into a vacuum chamber comprising a laser port
270 consisting of a ZnSe window fitted with a differentially pumped flange, and baked for
271 12 h at 150°C. Step-heating experiments were performed using a CO₂ laser beam (New
272 Wave Research MIR10–30 CO₂ laser system) defocused to a ~2 mm spot size and
273 slowly rastered over the sample. Steps were carried out at increasing laser power until
274 complete melting. Six feldspar grains from irradiation PAV-82, which were selected
275 among the largest and inclusion-free grains, were instead placed into a 3-mm diameter
276 of a copper holder and baked and incrementally heated as above. Ar isotope
277 concentrations are reported in Supplementary Table 2 and have been corrected for
278 blank, mass discrimination, radioactive decay and line blanks. Uncertainties on step
279 ages are 2 σ analytical uncertainties, including in-run statistics and uncertainties in the
280 discrimination factor, interference corrections and procedural blanks. Uncertainties on
281 the total gas ages and error-weighted means also include the uncertainty on the fluence
282 monitor (2 σ internal errors). Ages were calculated relative to an FCs age of 28.201
283 (Kuiper et al., 2008), which is consistent with an ACs age of 1.1848 Ma (Niespolo et
284 al., 2017), using decay constants recalculated by Min et al. (2001) and an atmospheric
285 $^{40}\text{Ar}/^{36}\text{Ar}$ ratio of 298.56 ± 0.31 (Lee et al., 2006).

286

287 4. Results

288 4.1 Deposit characteristics and stratigraphy

289 The summit portion of the Mount Melbourne volcano was surveyed during eleven
290 helicopter flights and seven fieldwork campaigns. Unfortunately, most of the volcano
291 is covered by snow and only a few summit exposures of the pyroclastic sequence
292 thought to be associated with the last eruptions are accessible for observation and
293 sampling. The uppermost pyroclastic succession was found in two small trenches dug
294 on the volcano flank (sections S1 and S5; Figs. 3 and 4), and in three natural exposures
295 hereafter named stratigraphic sections S2, S3 and S4 (Figs. 3 and 4). Some other
296 outcrops near the summit were visited and described but the exposure was limited and
297 insufficient to help constrain the event stratigraphy and aid interpretation of the
298 pyroclastic deposit sequence.

299 Section S1 was dug on the northern summit area (-74.34953 S, 164.69148 E) at an
300 altitude of 2605 m (Fig. 1). The pyroclastic succession is 40-60 cm-thick and consists
301 of massive, moderately sorted, clast-supported, and inversely graded pumice deposits
302 with clasts ranging from fine lapilli to bombs (Fig. 3a). The deposit is made of angular
303 to sub-angular highly vesicular, light-grey pumice lapilli and blocks with minor fine-
304 grained ash matrix (samples MELS1-2-3-4). Larger pumice bombs, up to 30 cm in
305 diameter, are concentrated in the topmost part of the sequence and often have broken
306 in situ and show a jigsaw-fit texture. Lithic fragments are rare and include dark grey
307 lava fragments and oxidized clasts as large as 6 cm (ML 4).

308 The sequence overlies a dark grey to black, ash and scoriaceous lapilli bed (sample
309 MELS1-1) that is >20 cm-thick (the base is not exposed), and it is capped by a
310 polymictic breccia mainly consisting of sparse pumice blocks and lapilli, dark to
311 reddish scoria fragments, and dense, variably altered lava clasts that are described in
312 detail in Giordano et al. (2012) (Fig. 3a). The dark scoriaceous bombs are up to 1 m in
313 diameter, occasionally have fluidal shapes and are scattered on the surface of the
314 deposit (sample MELS1-5; Fig. 4a).

315 Section S2 is located on the northeast slope of Mount Melbourne (-74.34933 S,
316 164.71756 E), at 2278 m of altitude (Fig. 1). The sequence is 210 cm thick and
317 comprises several stacked beds of clast-supported, ash-matrix-free, coarse pumiceous
318 lapilli, which alternate with alignments and lenses of pumice bombs (samples MELS2-
319 1-2-3-3bis-4) that are often bread-crust and up to 45 cm in diameter (Fig. 3b). In the
320 uppermost part of the section, the pumice lapilli deposit inversely grades into a c. 50
321 cm-thick bed made of decimeter-sized, dark brown to reddish pumice bombs (Fig. 3b).
322 Lithic fragments are present but scarce along the entire sequence and are mainly
323 represented by red-oxidized clasts and minor dark lava fragments that are <7 cm.

324 Section S3 comprises lenses and a massive deposit of centimeter-sized pumiceous
325 lapilli that is <1 m-thick (sample MELS3-1). These deposits are observed in
326 depressions and sheltered places on the top of a parasitic cone (1815 m of altitude) and
327 on the northern flank of Mount Melbourne (-74.3253 S, 164.6286 E; Fig. 4b and c).

328 Section S4 is exposed inside the northern wall of Mount Melbourne crater (-74.3506
329 S, 164.6994 E) at an elevation of 2526 m (Figs. 1 and 3c). It was described from a
330 distance as it is located in a quasi-vertical exposure. At this site, the pyroclastic
331 sequence is the thickest observed and is >15 m-thick (the base is not exposed). It is a
332 massive pumice lapilli unit with scattered bombs up to c. 30 cm in diameter (sample
333 MELS4-1). Like in section S2, the uppermost c. 1 m of the sequence comprises a dark
334 brown to reddish bed made of pumice bombs and blocks up to c. 1 m in diameter. This
335 unit is partially welded and it is capped by a lithic breccia comprising blocks to lapilli-
336 sized, black to orange-reddish moderately vesicular scoria and dense lava fragments
337 (Fig. 3c).

338 A black poorly sorted deposit, partially covered by snow, crops out on the surface in
339 the southern inner side of the crater. It is made of scoriaceous bombs (often
340 breadcrusted) and lapilli (sample MELS5-1) and overlies the massive pumice deposit
341 (-74.3578 S, 164.6994 E; Figs. 1 and 4d).

342

343 4.2 Clast textures and mineral compositions

Analysed samples from different pyroclastic units display distinctive textural, petrographic and geochemical features.

Sample MELS1-1 (Fig. 5a), which represents the lowermost stratigraphic unit, consists of porphyritic scoria with <500 µm euhedral phenocrysts and microphenocrysts of labradorite plagioclase (An₅₀₋₅₈), olivine (<110 µm; Fo₇₁), augite clinopyroxene (up to 80 µm; Wo₄₂-En₄₁-Fs₁₇), and Fe-Ti spinel (up to 60 µm), set in a dark glassy groundmass with abundant skeletal microlites of the same mineral phases. Some plagioclase phenocrysts display a reverse zoning pattern with sub-rounded anhedral cores of andesine composition (An₃₈).

Samples MELS1-2-3-4 (Section S1), MELS2-1-2-3-4 (Section S2), MELS3-1 (Section S3), and MELS4-1 (Section S4) represent the main pumice lapilli unit and show consistent textural and petrographic features across the different stratigraphic sections. These pumices (Fig. 5b) are highly vesicular, with spherical, tubular, and coalesced bubbles. In the majority of samples, the groundmass is glassy and clear, but the MELS2-4 and MELS4-1 samples have a light brown groundmass. In all pumice samples, the groundmass contains scarce euhedral to subhedral phenocrysts of feldspar up to 2 mm with anorthoclase to oligoclase compositions (An₁₆₋₂₇) (Supplementary Table 3). Some of the larger crystals occasionally show a sieve texture and most contain melt inclusions (Fig. 5b). Samples also contain phenocrysts of aegirine-augite clinopyroxene (up to 500 µm; Wo₄₅-En₂₀-Fs₃₅), olivine (Fo₁₅; up to 750 µm), Fe-Ti spinel (up to 200 µm) and apatite microphenocrysts (50 µm). Glomerophyres of plagioclase, clinopyroxenes, apatite and Fe-Ti oxides often occur.

Sample MELS1-5 (Section S1; Fig. 5c) is porphyritic scoria, containing sparse phenocrysts of oligoclase plagioclase (up to 750 µm; An₁₈₋₂₂), anhedral to subhedral Fe-rich olivine (up to 950 µm; Fo₁₅), Fe-augite clinopyroxene (up to 220 µm; Wo₄₄-En₂₁-Fs₃₅), Fe-Ti oxide (up to 170 µm), and minor apatite (up to 60 µm) in a brown cryptocrystalline groundmass with abundant acicular microlites of anorthoclase (Or₂₈) and minor glass.

372 Sample MELS5-1 (Section S1; Fig. 5d) is porphyritic scoria with abundant crystals of
373 plagioclase (up to 580 μm ; An_{22-37}) that plot across the boundary between andesine and
374 oligoclase in the ternary classification diagram of feldspars, olivine (up to 290 μm ;
375 Fo_{41}), augite clinopyroxene (up to 200 μm ; $\text{Wo}_{42}\text{-En}_{35}\text{-Fs}_{23}$) with oscillating zonation,
376 Fe-Ti oxide and apatite (up to 150 μm). Phenocrysts and microphenocrysts are
377 dispersed in a light brown, glassy groundmass containing scarce microlites of
378 plagioclase, clinopyroxene and Fe-Ti spinel.

379

380 *4.3 Major and trace element glass geochemistry*

381 The complete geochemical dataset including major, minor, and trace element glass
382 compositions is reported as Supplementary Material 1. Major oxides have been
383 recalculated to 100% on an anhydrous basis, and uncertainties are reported as 2
384 standard deviations (s.d.).

385 Sample MELS1-1 glass composition plots mainly in the trachybasalt field of the Total
386 Alkali versus Silica (TAS) diagram (LeBas et al., 1986; Fig. 6a, b) with some analyses
387 extending into the basaltic trachyandesite field (Fig. 6). The average SiO_2 content is
388 50.05 ± 0.69 wt.% and an alkali ($\text{Na}_2\text{O} + \text{K}_2\text{O}$) content between 5 and 7 wt.% with a low
389 alkali ratio ($\text{K}_2\text{O}/\text{Na}_2\text{O} = 0.60 \pm 0.07$). The average contents of the other major oxides
390 are 8.95 ± 0.50 wt.% CaO, 12.44 ± 1.09 wt.% FeO_{tot} , and 14.02 ± 0.35 wt.% Al_2O_3
391 (Fig. 6 and Supplementary Material 1).

392 Samples belonging to the main pumice lapilli deposit (MELS1-2-3-4 and MELS2-1-2-
393 3-4) exhibit extremely homogeneous major element glass compositions that plot in a
394 very narrow cluster within the trachyte field of the TAS diagram (LeBas et al., 1986;
395 Fig 6a, b). Average SiO_2 contents is 65.13 ± 0.31 wt.%, total alkali ($\text{Na}_2\text{O} + \text{K}_2\text{O}$)
396 content is 10.69 ± 0.28 wt.%, whilst the glasses display a low alkali ratio ($\text{K}_2\text{O}/\text{Na}_2\text{O}$
397 $= 0.86 \pm 0.03$). The average contents of other major oxides are 1.90 ± 0.20 wt.% CaO,
398 5.34 ± 0.15 wt.% FeO_{tot} , and 15.79 ± 0.28 wt.% Al_2O_3 (Fig. 6 and Supplementary
399 Material 1).

400 Sample MELS1-5 plots in a loose cluster within the trachyte field of the TAS diagram
 401 with a mean composition similar to those of samples from the main pumice deposits.
 402 The MELS1-5 glasses contain average major element contents of 64.8 ± 0.33 wt.%
 403 SiO_2 , 1.36 ± 0.37 wt.% CaO , 5.64 ± 0.36 wt.% FeOt , and 15.68 ± 0.45 wt. % Al_2O_3 ,
 404 which are very similar to those of the main pumice fall unit, however, these glasses
 405 have more variable total alkali contents that range between 10 and 13 wt.% (Fig. 6a, b
 406 and Supplementary Material 1).
 407 Finally, sample MELS5-1 is a homogeneous and trachytic in composition with an
 408 average SiO_2 content of 61.5 ± 0.26 wt.% and $\text{Na}_2\text{O} + \text{K}_2\text{O} = 10.30 \pm 0.12$ wt.% (Fig.
 409 6a, b). Other major oxides are also homogeneous with 2.77 ± 0.09 wt.% CaO , $8.14 \pm$
 410 0.19 wt.% FeO_{tot} , and 15.18 ± 0.24 wt.% Al_2O_3 (Fig. 6 and Supplementary Material 1).
 411 Consistent with the major element data, the samples of the main pyroclastic unit
 412 (MELS1-2, MELS1-3 and MELS2-1-2-3) show homogeneous trace element volcanic
 413 glass compositions. Multivariate trace elements compositional diagrams in Figure 7
 414 reveal homogeneous content of incompatible trace elements including Th (21 ± 0.5
 415 ppm), Y (55 ± 4 ppm), Zr (693 ± 40 ppm), Nb (165 ± 6 ppm), and the Rare Earth
 416 Elements (REE). Ratios of High Field Strength Elements (HFSE) to Th remain
 417 constant within the glasses analysed (e.g., Nb/Th = 8.05 ± 0.19 ; Ta/Th = 0.43; and
 418 Zr/Th = 33.7 ± 0.89). Sample averages normalized to the primitive mantle
 419 (McDonough and Sun, 1995) reveal that the volcanic glasses display enrichment in the
 420 Light REE relative to the Heavy REE where La/Yb = 19 ± 0.84 , while Sr (150 ± 12
 421 ppm) shows a pronounced negative anomaly (Sr/Pr_N = 7.13 ± 0.30 ; Fig. 8) along with
 422 Ba to a lesser extent, both diagnostic of feldspar fractionation (Fig. 8).
 423 Similar compositions also characterize sample MEL5-1 which is the highly porphyritic
 424 scoria on top of the main pumice fallout sequence. This sample shows very
 425 homogeneous trace element volcanic glass compositions with Th (22.5 ± 0.6 ppm), Y
 426 (63 ± 1.8 ppm), Zr (740 ± 21 ppm), Nb (182 ± 4 ppm), and the REE. Ratios of HFSE to
 427 Th remain constant within the glasses analysed (e.g. Nb/Th = 8.12 ± 0.11 ; Ta/Th =
 428 0.46; and Zr/Th = 33.05 ± 0.58) and are similar to the underlying pumice unit.

429 Conversely, sample MEL1-1, the trachybasaltic lapilli layer at the base of the main
430 pumice sequence, shows significantly lower levels of incompatible trace elements
431 enrichment. For instance Th (7.6 ± 1 ppm), Y (36 ± 4 ppm), Zr (312 ± 38 ppm), Nb
432 (82 ± 12 ppm), and the REE all display lower concentrations than the overlying
433 trachytes. This sample does show a positive anomaly in Sr (582 ± 31 ppm) and no
434 negative anomaly in Ba. (Fig. 8).

435

436 4.4 ^{40}Ar - ^{39}Ar data

437 ^{40}Ar - ^{39}Ar analysis on a feldspar separate (sample MELS1-3) was first acquired with an
438 old generation single-collector noble-gas mass spectrometer, which required a large
439 aliquot of separated mineral (tens of milligrams) corresponding to several tens of
440 grains. The step ages were also affected by very large analytical uncertainties, due to
441 the generally low radiogenic Ar content (Supplementary Table 2) and to the analytical
442 capabilities of the mass spectrometer. Step ages, although displaying enormous scatter
443 (from 271 ka to negative values, Fig. 9 and Supplementary Material 2), overlap within
444 analytical uncertainties and yield an apparent weighted mean age of 122 ± 33 ka, which
445 is in agreement with the total gas age of 140 ± 56 ka. K/Ca ratios, derived from neutron-
446 produced $^{39}\text{Ar}_\text{K}$ and $^{37}\text{Ar}_\text{Ca}$ isotopes, define an overall descending profile (Fig. 9),
447 ranging from 1.2 to 0.45, with a total gas K/Ca ratio of 0.61 ± 0.06 . Crystals from the
448 same mineral separate were later analyzed by a new generation multi-collector noble
449 gas spectrometer, which permitted analysis on a much smaller quantity of sample, in
450 the order of a few milligrams. This allowed selection of the largest (<2 mm), euhedral
451 and inclusion-free grains. The step-heating analysis yielded much more precise data,
452 with an overall descending age profile (Fig. 9), with ages ranging at face value from
453 45 to 4 ka. Excluding the first two steps, the remaining step age define a concordant
454 segment representing ~87% of the total $^{39}\text{Ar}_\text{K}$ released and yielding an apparent
455 weighted mean age of 13.5 ± 4.3 ka, in fairly good agreement with the total gas age of
456 17.3 ± 6.4 ka. K/Ca ratios, derived from neutron-produced Ar isotopes, define a gently
457 descending profile, from ~0.55 to ~0.39 (total gas K/Ca of 0.45 ± 0.05), significantly

458 lower than those from the step-heating experiment completed on the larger sample
459 aliquot.

460 In light of the petrographic observations and chemical data presented above on both
461 feldspar and glass from sample MELS1-3, more specifically the K/Ca measured in the
462 glass (mean 3.21 ± 0.14 , \pm SD, Supplementary Table 3) in the feldspar (mean 0.49 ± 0.11 ,
463 \pm SD, Supplementary Table 3), and attesting to the presence of glass inclusions in the
464 mineral separate, we assign the contrasting results between the two analyzed aliquots
465 to contamination by excess Ar (parentless ^{40}Ar) hosted in melt inclusions. The younger
466 ages observed for the smaller aliquot may be explained by a much less contaminated
467 sample, due to a better selection of the grain investigated. Strictly speaking, the
468 13.5 ± 4.3 ka age should be considered as a maximum estimate for the age for the fallout
469 pumice deposit.

470

471 **5. Discussion**

472 *5.1 Eruptive sequence and dynamics*

473 The pyroclastic sequence exposed on the summit part of Mount Melbourne starts with
474 the dark, trachybasaltic, scoriaceous lapilli and ash unit (Fig. 3a). The fine-grained,
475 massive and clast supported characteristics of the trachybasaltic scoriaceous lapilli and
476 texture of particles forming the deposit (sample MELS1-1) are consistent with a mildly
477 explosive Strombolian eruption (*eruption 1*) from a vent located in the summit area.
478 Trachybasaltic scoria deposits are directly in contact with the overlying pumice
479 trachytic lapilli sequence, and no trace of erosion is evident, nor altered volcaniclastic
480 material interposed between the two deposits. This suggests that both eruptions were
481 probably separated by a relatively short period of time (months/few years).

482 We interpret the thick pumice lapilli and bombs deposit and the lithic-rich breccia
483 (samples MELS1-2-3-4 and MELS2-1-2-3-4) as different parts of the same eruptive
484 event (*eruption 2*; Fig. 10). The pumice lapilli and bombs unit is interpreted as a fallout
485 deposit (as it comprised of multiple massive, clast-supported pumice beds of unabraded

angular to sub-angular fragments that often have an in situ jigsaw-fit texture) erupted during the acme of an intense highly explosive eruption. The multiple cycles of reverse grading that characterizes the unit potentially reflects variations in the plume height and the intensity of the eruption during the waxing and waning of a pulsating column or could be linked to changes in the wind direction (Wilson et al., 1980). The lithic-rich breccia on top of the sequence associated with partially welded m-sized pumice bombs and blocks could indicate that after the emplacement of the main lapilli unit, there was an erosion of the vent walls or crater collapse. Widening or collapsing of the vent with the consequent incorporation of a dense lithic fraction should have led to an increase in the eruptive plume density and finally to its collapse and the deposition of the coarse-grained, proximal lithic and pumice-rich breccia. Similar deposits corresponding to proximal lag breccias or a crater collapse breccia (see Walker 1985) are quite widespread in deposits associated with large caldera collapse (Druitt and Bacon, 1986; Bear et al., 2009). Armienti et al. (1991) proposed that the Mount Melbourne crater is a small caldera, but they did not provide supporting evidence. It is not possible to know if the studied pyroclastic sequence ended with the emplacement of the lithic breccia. However, our observations indicate no evidence of significant erosion, so we hypothesize that it was erupted during the final stages of activity. Also Vulcanian-style explosive eruptions can produce massive heterolithic breccias made of angular, accessory lithics of various nature with minor accidental juvenile fragments. Thus, a second hypothesis may be that the lithic-rich breccia on top of the sequence is the result of a discrete Vulcanian explosion that occurred after the cessation of the main eruptive sequence.

The summit deposits described by Wörner et al. (1989), Wörner and Viereck (1990), and Giordano et al. (2012) are similar to those studied here by us in our in section S4. They report that along the rim of the summit crater the ground is covered by an accumulation of dark grey juvenile lapilli, <70 cm-thick punctuated by scattered bombs up to 50 cm in diameter, plus abundant polymictic lithic blocks. The deposit is interpreted as a coarse-grained fallout possibly related to the last explosive eruption of

515 Mount Melbourne. In the crater wall, this deposit overlies, with a gradational transition,
 516 a >15 m-thick pumice lapilli fallout deposit. The limited number of exposures hampers
 517 the reconstruction of isopach, isomass and isopleth maps and hinders retrieval of the
 518 key physical parameters of the eruption, such as the erupted volume and mass, plume
 519 height, and mass discharge rate. Inferences on the eruption intensity can be made only
 520 on the basis of the thickness and architecture of the deposit in the proximal facies,
 521 which suggest a sub-Plinian to Plinian eruption. On the basis of ^{40}Ar - ^{39}Ar data, the age
 522 of this eruption is $\leq 13.5 \pm 4.3$ ka. In the northern sector of the summit area of Mount
 523 Melbourne, the top of trachytic pumice lapilli unit has scattered dark volcanic blocks
 524 and bombs that are up to c. 50 cm in diameter and trachytic in composition (sample
 525 MELS1-5; Figs. 4a and 10). This deposit potentially represents the products of a small-
 526 scale eruption possibly of Strombolian or Vulcanian style (*eruption 3*) that occurred
 527 just after the sub-Plinian/Plinian eruption (*eruption 2*). Alternatively, also considering
 528 that the geochemical composition of the two deposits is quite similar, the latter could
 529 represent a late phase of the previous *eruption 2*.
 530 Finally, according to their characteristics, the scoria lapilli and bombs of trachytic
 531 composition, recovered in the southern sector of the caldera (Fig. 4d and 10; sample
 532 MELS5-1), can be interpreted as deriving from another eruption and could be linked
 533 to the formation of one of the scoria cones/fissures in the southern sector of the caldera
 534 (*eruption 4*). Considering the deposit characteristics (e.g. structure, thickness, and
 535 distribution) the eruption must have been energy significantly lower than that of
 536 *eruption 2*. This eruption occurred after the large sub-Plinian/Plinian eruption (*eruption*
 537 *2*) that deposited the main sequence of trachytic pumiceous lapilli; conversely, we
 538 cannot constrain the chronological relationship with the deposits of *eruption 3* in the
 539 northern sector of the summit area of Mount Melbourne because exposures do not show
 540 them in direct stratigraphic contact.
 541 The studied deposits have glass geochemical compositions ranging from trachybasalt
 542 to trachyte (Fig. 6a). Samples plot on a well-defined compositional trend typical of
 543 products of Mount Melbourne (Lee et al., 2019; Rocchi and Smellie, 2021). The less

544 evolved trachybasalt-basaltic trachyandesite compositions are observed in the
545 stratigraphically lowermost sample (MELS1-1), while the later samples are all evolved
546 and trachytic in composition (MELS2-1-2-3-4 and MELS1-5);
547 From a geochemical point of view, the studied sample show homogeneous major and
548 trace element glass compositions, both within and between deposits. Only the MELS1-
549 1 (trachybasalt-basaltic trachyandesite) and MELS1-5 (trachyte) samples have glass
550 compositions that display wide internal variation in the alkali contents, which could be
551 related to late stage crystallization of microlites that vary in abundance. No mineralogic
552 or geochemical evidence of significant magma mingling/mixing occurs (e.g. banded
553 clasts or mixing/mingling texture in mineral phases). Mineral phases are fairly
554 homogeneous in composition although some feldspar crystals show sieve textures,
555 which indicate they were not in continuous equilibrium in the magmatic system and
556 suggest the system was recharged or they were incorporated as antecrysts during
557 crystallization. In general, each eruption was fed by a relatively homogeneous melt.

558

559 *5.3 Proximal-distal correlation*

560 The trachytic pumices from MELS2-1-2-3-4 and MELS1-5 in the main pyroclastic unit
561 (*eruption 2*) are geochemically indistinguishable from the compositions of tephra
562 previously sampled on the eastern flanks of Mount Melbourne and in particular with
563 MMTep004, 005, 007, 008, and 020 of Lee and Lee (2017), and samples A1602, 1604
564 and 1605 of Lee et al. (2019). This suggests that the samples of Lee and Lee (2017)
565 and Lee et al. (2019) possibly derive from the same eruptions studied here.

566 To test the possible correlation between studied deposits and other proximal deposits
567 of Mount Melbourne with more distal tephra layers found in records of Antarctica we
568 compared the major- and trace-element (when available) compositions with those of
569 tephra layers found in ice cores, marine sediments, blue ice and continental outcrops
570 (Figs. 6 and 7). We dedicated special attention to tephra layers found in the Talos
571 Dome, Styx Glacier and GV7 ice cores, as well as Frontier Mountain and Brimstone
572 Peak blue-ice fields records since they are the closest sites to Mount Melbourne

volcano and thus the best candidates to host tephra and cryptotephra derived from the studied eruptions. Talos Dome is located at c. 250 km from Mount Melbourne, Styx Glacier c. 100 km and GV7 ice core site c. 350 km, whereas Frontier Mountain and Brimstone Peak blue-ice fields are c. 210 and 190 km, respectively. Considering the apparent age of $\leq 13.5 \pm 4.3$ ka of the main sub-Plinian/Plinian eruption studied here, we limited the research to the c. 18 ka to the recent.

A compositional similarity exists between the glass composition of trachy-basaltic deposits representative of the older eruption studied here (*eruption 1*), Talos Dome glass shards concentrations TD238a (237.31 m) and TD388-2b (387.76 m). The latter have ages of 2684 ± 47 a BP and 5277 ± 49 a BP, respectively (Severi et al., 2012; Narcisi et al., 2012), and are attributed to Mount Melbourne by Narcisi et al. (2012). A broad compositional affinity also exists between the glass composition of the main trachytic pumice deposit (*eruption 2*) and many tephra and cryptotephra layers found at different depths in the ice core record of Talos Dome. These include TD85 (84.37 m), TD210 (209.50 m), TD238b (237.31 m), TD388 (387.76 m), and TD662 (661.86 m), that correspond to a wide age interval between 670 ± 7 a BP and $11,364 \pm 132$ a BP (Severi et al., 2012). Among these layers, the greatest geochemical similarities occur with the TD85 tephra layer (Fig. 6) which was dated at 670 ± 7 yrs BP (or 1280 ± 7 C.E.) by Severi et al. (2012) and is attributed to Mount Melbourne by Narcisi et al. (2012). Despite the geochemical similarities, the significant age difference with the TD85 tephra and the age determined for *eruption 2* (13.5 ± 4.3 ka) makes their correlation unlikely. A good compositional match also occurs between the deposits of *eruption 2* (samples MELS1-2-3-4 and MELS2-1-2-3-4) and a shard population in sample SDMA-9007, which represents a visible 1 mm thick tephra layer found at a depth of 539.012 m in the Siple Dome ice record. The latter is predominantly rhyolitic in composition and dated at 9355 ± 2 yrs BP (Kurbatov et al., 2006). In this case, however, our age determination for *eruption 2* (13.5 ± 4.3 ka) is indistinguishable within 2σ error limits. Unfortunately, there are no single shard laser ablation trace element data for this tephra, and there are only data for selected samples in the 16.5 and 71 ka age interval

for Talos Dome (see Narcisi et al., 2012). Trace element glass compositions for the Last Glacial to Holocene age interval are required to make robust correlations. No compositional similarity exists between trachytic sample MELS5-1 representative of the youngest eruption of Mount Melbourne studied (*eruption 4*) and any currently analyzed tephra and cryptotephra found in the Talos Dome ice core or other ice records around Mount Melbourne volcano. However, the closest ice records to Mount Melbourne only span a limited timeframe, with the Styx Glacier spanning the last c. 1800 yrs (Yang et al. 2018; Kim et al. 2020) and GV7 only spanning the last c. 1000 yrs (Nardin et al. 2021). The comparison between the proximal deposits of Mount Melbourne (Lee and Lee, 2017; Lee et al., 2019; this work), and tephra in the glacial record clearly shows that there is no correlation between the proximal pyroclastic deposits and the distal tephra in the glacial archives that were previously attributed to Mount Melbourne. For instance, in the glacial record of Talos Dome, most of tephra or cryptotephra identified in the last c. 15 ka (total of 23 layers) have been attributed to the Mount Melbourne volcano area (Narcisi et al., 2012), but there is only evidence for four explosive eruptions around the summit of the volcano (Lee et al. 2020a, b; this work). Of these eruptions, only one of the deposits (*eruption 2*) displays features that are typically associated with eruptions that produce far-travelled ash and could have potentially reached the Talos Dome site. The other three eruptions possibly had mild Strombolian dynamics or were discrete Vulcanian explosions with energy arguably less compatible with producing ash layers as far as 250 km from the source. Two hypotheses can explain this discrepancy: i) the record of proximal pyroclastic deposits is very fragmented due to erosion and/or glacial cover, and is not fully representative of the activity of Mount Melbourne. This seems questionable because eruptions capable of depositing ash layers at considerable distances from the source would emplace thick pyroclastic sequences in the proximal areas (even if other deposits could be present at deeper levels but unexposed). Alternatively, ii) many of the tephra and cryptotephra previously attributed to Mount Melbourne were sourced from different volcanoes, despite erupting trachytic compositions that are similar to those of Mount

Melbourne. This again highlights that high-quality electron microprobe and trace element compositions of representative samples for the proximal deposits and distal tephra layers are needed for reliable correlation and the synchronization of tephra archives. In particular, trace element compositions are invaluable for the reliable identification of volcanic sources, and specific eruption deposits, especially for sequential eruptions that have similar major element compositions and to identify temporal and spatial petrological and geochemical variations in pyroclastic rocks from Antarctica.

639

6 Conclusions

Stratigraphic, mineralogical and geochemical characterization of deposits exposed around Mount Melbourne has improved our understanding of the eruptive history of this volcano. We recognized four different deposits in well-defined stratigraphic positions that are characterized by different textures, mineralogies, and geochemical compositions. These deposits correspond to four explosive eruptions (*eruptions 1, 2, 3 and 4*), ranging from Strombolian/Vulcanian to sub-Plinian/Plinian, and with compositions from trachy-basaltic to trachytic perfectly matching with the composition of the Mount Melbourne products that were previously reported by Lee and Lee, (2017) and Lee et al. (2019).

On the basis of the ^{40}Ar - ^{39}Ar laser data, the age of the largest of the recognized eruptions that deposited a very thick fallout of trachytic pumice is $\leq 13.5 \pm 4.3$ ka which is likely to be a maximum estimate. Another age-based determination from a less advanced analytical instrument suggests an older age and probably the result of considerable contamination by xenocrysts.

Based on the comparison between the glass compositions in the studied deposits and that in englacial tephra layers found in ice cores around Mount Melbourne we can conclude that Mount Melbourne is the likely source for many of the tephra and ash particles identified. Unfortunately, there are no clear correlations between proximal and distal deposits so the dates of the eruptions are uncertain. For example, the glass

660 compositions of several proximal tephra on Mount Melbourne are similar to tephra
661 layers recovered in Talos Dome and Siple Dome ice cores records. In particular, a good
662 geochemical match exists between the glass composition of the main trachytic pumice
663 at Mount Melbourne with TD85 tephra layer in Talos Dome that is too young (670 ± 7
664 yrs BP), and a geochemical population of the SDMA-9007 visible tephra layer found
665 in Siple Dome ice record that is dated at 9355 ± 2 yrs BP and falls in the age interval of
666 *eruption 2*. To facilitate reliable correlations and synchronization of tephra archives,
667 high-quality electron microprobe and trace element compositions of representative
668 samples are required.

669 Mount Melbourne is an active volcano and a potential danger for the nearby scientific
670 stations and aviation safety across Antarctica. The permanent settlement and seasonal
671 presence of scientists, technicians, tourists and logistical personnel close to this active
672 volcano have increased significantly in the last decades. Given that the last eruptions
673 were explosive and associated with evolved magma compositions, sub-Plinian/Plinian
674 explosive activity could potentially occur in the future. Moreover, the presence of ice
675 enhances the risk of hydrovolcanic eruptions, which due to magma–water interaction
676 could turn small volume eruptions into highly explosive ash-forming events (e.g. White
677 and Houghton, 2006). The monitoring network that is set up around Mount Melbourne
678 is thus essential to assess signs of unrest.

679

680 **Acknowledgements**

681 This work was funded by the Projects: ICE-VOLC (multiparametrIC Experiment at
682 Antarctica VOLCanoes: data from volcano and cryosphere-ocean-atmosphere
683 dynamics, www.icevolc-project.com/data; PNRA 14_00011) and TRACERS
684 (TephRoChronology and mArker events for the CorrElation of natural archives in the
685 Ross Sea, Antarctica; PNRA2016 - Linea A3/00055). We acknowledge PNRA, the
686 Italian *Programma Nazionale di Ricerche in Antartide*, for funding the projects and
687 ENEA for providing field logistics at Mario Zucchelli Station. We are grateful to the
688 pilots J. Henery and B. McElhinney for helicopter surveys and the INGV-OE colleague

689 G. Larocca and Italian alpine guide D. De Podestà for their help in the fieldwork. Dr.
690 C. Manning is also acknowledgement for assistance with the LA-ICP-MS analysis.
691 This paper is sponsored by the SCAR Expert Group, AntVolc. We would like to
692 sincerely thank Prof. J.L. Smellie and another anonymous reviewer for detailed and
693 constructive comments and suggestions that improved this manuscript.

694

695 **References**

696 Adamson, R.G., Cavaney, R.J., 1967. Volcanic Debris-Layers near Mount Melbourne,
697 Northern Victoria Land, Antarctica. New Zeal. J. Geol. Geophys. 10, 418–421.
698 <https://doi.org/10.1080/00288306.1967.10426745>

699 Armienti, P., Civetta, L., Innocenti, F., Manetti, P., Tripodo, S., Villari, L., Vita, G.,
700 1991. New petrological and geochemical data on Mt. Melbourne Volcanic Field,
701 Northern Victoria Land, Antarctica. (II Italian Antarctic Expedition). Mem. Soc. Geol.
702 It., 46, 397-424

703 Armstrong, R.L., 1978. K-Ar dating: Late Cenozoic McMurdo Volcanic Group and
704 dry valley glacial history, Victoria Land, Antarctica. New Zeal. J. Geol. Geophys. 21,
705 685–698. <https://doi.org/10.1080/00288306.1978.10425199>

706 Bear, A.N., Cas, R.A.F., Giordano, G. 2009. The implications of spatter, pumice and
707 lithic clast rich proximal co-ignimbrite lag breccias on the dynamics of caldera forming
708 eruptions: The 151 ka Sutri eruption, Vico Volcano, Central Italy. J. Volcanol.
709 Geotherm. Res. 181(1-2), 1-24. <https://doi.org/10.1016/j.jvolgeores.2008.11.032>

710 Bonaccorso A, Gambino S., Falzone G., Privitera E., 1997. The volcanological
711 observatory of the Mt. Melbourne (Northern Victoria Land, Antarctica). In: "The
712 Antarctic Region: Geological evolution and processes", C.A. Ricci (Ed.), Terra
713 Antartica Publication, Siena, 1083-1086.

714 Del Carlo, P., Di Roberto, A., Di Vincenzo, G., Bertagnini, A., Landi, P., Pompilio,
715 M., Colizza, E., Giordano, G., 2015. Late Pleistocene-Holocene volcanic activity in

716 northern Victoria Land recorded in Ross Sea (Antarctica) marine sediments. Bull.
 717 Volcanol. 77, 36. <https://doi.org/10.1007/s00445-015-0924-0>

718 Di Roberto, A., Colizza, E., Del Carlo, P., Petrelli, M., Finocchiaro, F., Kuhn, G., 2019.
 719 First marine cryptotephra in Antarctica found in sediments of the western Ross Sea
 720 correlates with englacial tephtras and climate records. Sci. Rep. 9, 10628.
 721 <https://doi.org/10.1038/s41598-019-47188-3>

722 Di Roberto, A., Albert, P.G., Colizza, E., Del Carlo, P., Di Vincenzo, G., Gallerani, A.,
 723 Giglio, F., Kuhn, G., Macrì, P., Manning, C.J., Melis, R., Miserochi, S., Scateni, B.,
 724 Smith, V.C., Torricella, F., Winkler, A., 2020. Evidence for a large-magnitude
 725 Holocene eruption of Mount Rittmann (Antarctica): A volcanological reconstruction
 726 using the marine tephra record. Quat. Sci. Rev. 250, 106629.
 727 <https://doi.org/https://doi.org/10.1016/j.quascirev.2020.106629>

728 Di Roberto, A., Scateni, B., Di Vincenzo, G., Petrelli, M., Fisauli, G., Barker, S.J., Del
 729 Carlo, P., Colleoni, F., Kulhanek, D.K., McKay, R., De Santis, L., The IODP
 730 Expedition 374 Scientific Party, 2021a. Tephrochronology and Provenance of an Early
 731 Pleistocene (Calabrian) Tephra From IODP Expedition 374 Site U1524, Ross Sea
 732 (Antarctica). Geochemistry, Geophys. Geosystems 22, e2021GC009739.
 733 <https://doi.org/https://doi.org/10.1029/2021GC009739>

734 Di Roberto, A., Del Carlo, P., Pompilio, M., 2021b. Chapter 6.1 Marine record of
 735 Antarctic volcanism from drill cores. Geol. Soc. London, Mem. 55, 631 LP – 647.
 736 <https://doi.org/10.1144/M55-2018-49>

737 Di Vincenzo, G., Folco, L., Suttle, M.D., Brase, L., Harvey, R.P., 2021. Multi-collector
 738 $^{40}\text{Ar}/^{39}\text{Ar}$ dating of microtektites from Transantarctic Mountains (Antarctica): A
 739 definitive link with the Australasian tektite/microtektite strewn field. Geochim.
 740 Cosmochim. Acta 298, 112–130.
 741 <https://doi.org/https://doi.org/10.1016/j.gca.2021.01.046>

742 Druitt, T.H., Bacon, C.R. 1986. Lithic breccia and ignimbrite erupted during the
 743 collapse of Crater Lake Caldera, Oregon. *J. Volcanol. Geotherm. Res.* 29(1-4), 1-32.
 744 [https://doi.org/10.1016/0377-0273\(86\)90038-7](https://doi.org/10.1016/0377-0273(86)90038-7)

745 Gambino, S., Armienti, P., Cannata, A., Del Carlo, P., Giudice, G., Giuffrida, G.,
 746 Liuzzo, M., Pompilio, M., 2021. Chapter 7.3 Mount Melbourne and Mount Rittmann.
 747 *Geol. Soc. London, Mem.* 55, M55-2018–43. <https://doi.org/10.1144/M55-2018-43>

748 Geyer, A., Marti, A., Giralt, S., Folch, A., 2017. Potential ash impact from Antarctic
 749 volcanoes: Insights from Deception Island’s most recent eruption. *Sci. Rep.* 7, 16534.
 750 <https://doi.org/10.1038/s41598-017-16630-9>

751 Geyer, A., 2021. Chapter 1.4 Antarctic volcanism: active volcanism overview. *Geol.*
 752 *Soc. London, Mem.* 55, M55-2020–12. <https://doi.org/10.1144/M55-2020-12>

753 Geyer, A., Pedrazzi, D., Almendros, J., Berrocoso, M., López-Martínez, J., Maestro,
 754 A., Carmona, E., Álvarez-Valero, A.M., de Gil, A., 2021. Chapter 7.1 Deception
 755 Island. *Geol. Soc. London, Mem.* 55, M55-2018–56. [https://doi.org/10.1144/M55-](https://doi.org/10.1144/M55-2018-56)
 756 [2018-56](https://doi.org/10.1144/M55-2018-56)

757 Giordano, G., Lucci, F., Phillips, D., Cozzupoli, D., Runci, V., 2012. Stratigraphy,
 758 geochronology and evolution of the Mt. Melbourne volcanic field (North Victoria
 759 Land, Antarctica). *Bull. Volcanol.* 74, 1985–2005. [https://doi.org/10.1007/s00445-](https://doi.org/10.1007/s00445-012-0643-8)
 760 [012-0643-8](https://doi.org/10.1007/s00445-012-0643-8)

761 Harpel, C.J., Kyle, P.R., Dunbar, N.W., 2008. Englacial tephrostratigraphy of Erebus
 762 volcano, Antarctica. *J. Volcanol. Geoth. Res.* 177, 549e568.
 763 <https://doi.org/10.1016/j.jvolgeores.2008.06.001>.

764 Iverson, N.A., Kyle, P.R., Dunbar, N.W., McIntosh, W.C., Pearce, N.J.G., 2014.
 765 Eruptive history and magmatic stability of Erebus volcano, Antarctica: Insights from

766 englacial tephra. *Geochemistry, Geophys. Geosystems* 15, 4180–4202.
 767 <https://doi.org/https://doi.org/10.1002/2014GC005435>

768 Jochum, K.P., Pfänder, J., Woodhead, J.D., Willbold, M., Stoll, B., Herwig, K., Amini,
 769 M., Abouchami, W., Hofmann, A.W., 2005. MPI-DING glasses: New geological
 770 reference materials for in situ Pb isotope analysis. *Geochemistry, Geophys.*
 771 *Geosystems* 6. <https://doi.org/https://doi.org/10.1029/2005GC000995>

772 Kim, D., Prior, D.J., Han, Y., Qi, C., Han, H., Ju, H.T., 2020. Microstructures and
 773 Fabric Transitions of Natural Ice from the Styx Glacier, Northern Victoria Land,
 774 Antarctica. *Minerals* 10, 892. <https://doi.org/10.3390/min10100892>

775 Kuiper, K.F., Deino, A., Hilgen, F.J., Krijgsman, W., Renne, P.R., Wijbrans, J.R.,
 776 2008. Synchronizing Rock Clocks of Earth History. *Science*, 320, 500–504.
 777 <https://doi.org/10.1126/science.1154339>

778 Kurbatov, A. V, Zielinski, G.A., Dunbar, N.W., Mayewski, P.A., Meyerson, E.A.,
 779 Sneed, S.B., Taylor, K.C., 2006. A 12,000 year record of explosive volcanism in the
 780 Siple Dome Ice Core, West Antarctica. *J. Geophys. Res.*, 111, D12307.
 781 <https://doi.org/https://doi.org/10.1029/2005JD006072>

782 LeBas, M.J.L., Maitre, R.W.L., Streckeisen, A., Zanettin, B., IUGS Subcommission
 783 on the Systematics of Igneous Rocks, 1986. A Chemical Classification of Volcanic
 784 Rocks Based on the Total Alkali-Silica Diagram. *J. Petrol.* 27, 745–750.
 785 <https://doi.org/10.1093/petrology/27.3.745>

786 Lee, J.-Y., Marti, K., Severinghaus, J.P., Kawamura, K., Yoo, H.-S., Lee, J.B., Kim,
 787 J.S., 2006. A redetermination of the isotopic abundances of atmospheric Ar. *Geochim.*
 788 *Cosmochim. Acta* 70, 4507–4512.
 789 <https://doi.org/https://doi.org/10.1016/j.gca.2006.06.1563>

790 Lee, M.J., Lee, J.I., 2017. Holocene eruptive history of Mt. Melbourne volcano,
 791 Antarctica: insights from tephra layers recorded from Talos Dome ice core. *J. Geol.*
 792 *Soc. Korea*, 53(4) 509-519. <https://doi.org/10.14770/jgsk.2017.53.4.509>

793 Lee, M.J., Kyle, P.R., Iverson, N.A., Lee, J.I., Han, Y., 2019. Rittmann volcano,
 794 Antarctica as the source of a widespread 1252 ± 2 CE tephra layer in Antarctica ice.
 795 *Earth Planet. Sci. Lett.* 521, 169–176. <https://doi.org/10.1016/j.epsl.2019.06.002>

796 Lee, M.J., Kim, G.B., Kyle, P.R., Lee, J.I., 2020a. Holocene eruption episodes of Mt.
 797 Melbourne, Antarctica: Constraints from proximal-distal tephra correlations.
 798 *Goldschmidt 2020 Abstract* <https://doi.org/10.46427/gold2020.1439>

799 Lee, J.I., Lee, M.J., Kim, G.B., Kyle, P.R., 2020b. Petrology of the most recent
 800 eruptions of Melbourne Volcano, Antarctica: insights into evolution of the magma
 801 plumbing system. *Goldschmidt 2020 Abstract* <https://doi.org/10.46427/gold2020.1435>

802 Lyon, G.L., 1986. Stable isotope stratigraphy of ice cores and the age of the last
 803 eruption at Mount Melbourne, Antarctica. *New Zeal. J. Geol. Geophys.* 29, 135–138.
 804 <https://doi.org/10.1080/00288306.1986.10427528>

805 McDonough, W.F., Sun, S.-s., 1995. The composition of the Earth. *Chem. Geol.* 120,
 806 223–253. [https://doi.org/https://doi.org/10.1016/0009-2541\(94\)00140-4](https://doi.org/https://doi.org/10.1016/0009-2541(94)00140-4)

807 Min, K., Mundil, R., Renne, P.R., Ludwig, K.R., 2000. A test for systematic errors in
 808 $^{40}\text{Ar}/^{39}\text{Ar}$ geochronology through comparison with U/Pb analysis of a 1.1-Ga
 809 rhyolite. *Geochim. Cosmochim. Acta* 64, 73–98.
 810 [https://doi.org/https://doi.org/10.1016/S0016-7037\(99\)00204-5](https://doi.org/https://doi.org/10.1016/S0016-7037(99)00204-5)

811 Narcisi, B., Petit, J.R., Chappellaz, J., 2010. A 70 ka record of explosive eruptions from
 812 the TALDICE ice core (Talos Dome, East Antarctic plateau). *J. Quat. Sci.* 25, 844–
 813 849. <https://doi.org/https://doi.org/10.1002/jqs.1427>

814 Narcisi, B., Petit, J.R., Delmonte, B., Scarchilli, C., Stenni, B., 2012. A 16,000-yr
815 tephra framework for the Antarctic ice sheet: a contribution from the new Talos Dome
816 core. *Quat. Sci. Rev.* 49, 52–63.
817 <https://doi.org/https://doi.org/10.1016/j.quascirev.2012.06.011>

818 Narcisi, B., Petit, J.R., 2021. Chapter 6.2 Englacial tephras of East Antarctica. *Geol.*
819 *Soc. London, Mem.* 55, 649 LP – 664. <https://doi.org/10.1144/M55-2018-86>

820 Nardin, R., Severi, M., Amore, A., Becagli, S., Burgay, F., Caiazzo, L., Ciardini, V.,
821 Dreossi, G., Frezzotti, M., Hong, S.-B., Khan, I., Narcisi, B.M., Proposito, M.,
822 Scarchilli, C., Selmo, E., Spolaor, A., Stenni, B., Traversi, R., 2021. Dating of an East
823 Antarctic ice core (GV7) by high resolution chemical stratigraphies. *Clim. Past*
824 *Discuss.* 2021, 1–27. <https://doi.org/10.5194/cp-2021-44>

825 Niespolo, E.M., Rutte, D., Deino, A.L., Renne, P.R., 2017. Intercalibration and age of
826 the Alder Creek sanidine $^{40}\text{Ar}/^{39}\text{Ar}$ standard. *Quat. Geochronol.* 39, 205–213.
827 <https://doi.org/10.1016/j.quageo.2016.09.004>

828 Rocchi, S., Smellie, J.L., 2021. Chapter 5.1b Northern Victoria Land: petrology. *Geol.*
829 *Soc. London, Mem.* 55, 383 LP – 413. <https://doi.org/10.1144/M55-2019-19>

830 Sims, K.W.W, Aster, R.C, Gaetani, G., Blichert-Toft, J., Phillips, E.H., Wallace, P.J.,
831 Mattioli, G.S., Rasmussen, D., Boyd, E.S., 2021. Chapter 7.2 Mount Erebus. *Geol.*
832 *Soc. London, Mem.* 55, 695-739. <https://doi.org/10.1144/M55-2019-8>

833 Severi, M., Udisti, R., Becagli, S., Stenni, B., Traversi, R., 2012. Volcanic
834 synchronisation of the EPICA-DC and TALDICE ice cores for the last 42 kyr BP.
835 *Clim. Past* 8, 509–517. <https://doi.org/10.5194/cp-8-509-2012>

836 Smellie, J.L., Rocchi, S. 2021. Chapter 5.1a Northern Victoria Land: volcanology. *Soc.*
837 *London, Mem.* 55(1), 347. <http://dx.doi.org/10.1144/M55-2018-60>

- 838 Sun, S.-s., McDonough, W.F., 1989. Chemical and isotopic systematics of oceanic
839 basalts: implications for mantle composition and processes. *Geol. Soc. London, Spec.*
840 *Publ.* 42, 313 LP – 345. <https://doi.org/10.1144/GSL.SP.1989.042.01.19>
- 841 Tomlinson, E.L., Thordarson, T., Müller, W., Thirlwall, M., Menzies, M.A., 2010.
842 Microanalysis of tephra by LA-ICP-MS - Strategies, advantages and limitations
843 assessed using the Thorsmörk ignimbrite (Southern Iceland). *Chem. Geol.* 279, 73–89.
844 <https://doi.org/10.1016/j.chemgeo.2010.09.013>
- 845 Walker, G.P.L. 1985. Origin of coarse lithic breccias near ignimbrite source vents. *J.*
846 *Volcanol. Geotherm. Res.* 25(1–2), 157-171. [https://doi.org/10.1016/0377-](https://doi.org/10.1016/0377-0273(85)90010-1)
847 [0273\(85\)90010-1](https://doi.org/10.1016/0377-0273(85)90010-1).
- 848 White, J.D.L., Houghton, B.F., 2006. Primary volcanoclastic rocks. *Geology*, 34, 677–
849 680. <https://doi.org/10.1130/G22346.1>
- 850 Wilson, L., Sparks, R.S.J., Walker, G.P.L., 1980. Explosive volcanic eruptions — IV.
851 The control of magma properties and conduit geometry on eruption column behaviour.
852 *Geophys. J. Int.* 63, 117–148. <https://doi.org/10.1111/j.1365-246X.1980.tb02613.x>
- 853 Wörner, G., Viereck, L., 1990. Individual Volcano Descriptions A10: Mt. Melbourne.
854 *Antarct. Res. Ser.*, 48, 72-78.
- 855 Wörner, G., Viereck, L., Hertogen, J., Niephaus, H., 1989. The Mt. Melbourne
856 Volcanic Field (Victoria Land, Antarctica) II: Geochemistry and magma genesis.
857 *Geologisches Jahrbuch E*, 38, 395-433
- 858 Yang, J.-W., Han, Y., Orsi, A.J., Kim, S.-J., Han, H., Ryu, Y., Jang, Y., Moon, J., Choi,
859 T., Hur, S. Do, Ahn, J., 2018. Surface Temperature in Twentieth Century at the Styx
860 Glacier, Northern Victoria Land, Antarctica, From Borehole Thermometry. *Geophys.*
861 *Res. Lett.* 45, 9834–9842. <https://doi.org/https://doi.org/10.1029/2018GL078770>

862
863 **Captions**

864 Figure 1. (A) Map of Antarctica showing the locations of Mount Melbourne volcano
865 and Antarctic deep and shallow ice cores and blue ice field (circles). (B) Map of Mount
866 Melbourne and locations of the studied stratigraphic sections (S1-S5).

867 Figure 2. A) Picture of Mount Melbourne taken from Mario Zucchelli Station located
868 about 40 km south of the volcano; B) the bottom of the summit crater filled by snow
869 and the rim is observed on the left of the picture. In the background, two scoria cones
870 are visible.

871 Figure 3. Pictures and schematic logs of the stratigraphic sections S1, S2 and S4.

872 Figure 4. Pictures of: A) northern summit area covered by black bombs that range from
873 around a meter to centimeters in size (sample MELS1-5); B) a parasitic scoria cone in
874 the northern flank of Mount Melbourne; C) trachytic pumice deposit exposed at the top
875 of the parasitic scoria cone in B (section S3); D) small outcrop of the scoria deposit
876 covered by snow, which is located in the southern side of the summit crater (section
877 S5; sample MELS5-1).

878 Figure 5. SEM backscatter images of studied products showing textural features of
879 Mount Melbourne volcanic products. A) Sample MELS1-1 is a porphyritic scoria from
880 the lowermost lapilli deposit; it consists of phenocrysts of plagioclase in a glassy
881 groundmass rich of skeletal microlites; B) Sample MELS1-3 represents a pumice of
882 the main pyroclastic fallout unit; it has highly vesicular and glassy groundmass with
883 phenocrysts of feldspars showing sieve texture; C) Sample MELS1-5 represents
884 scoriaceous bombs scattered over the pumice deposit; it is a low porphyritic scoria with
885 phenocrysts dispersed in a groundmass with abundant acicular microlites of feldspar;
886 D) Sample MELS5-1 represents the scoriaceous bombs and lapilli overlaying the
887 pumice deposits; it is a high porphyritic scoria with abundant phenocrysts in a glassy
888 groundmass.

889 Figure 6. Major element glass geochemical variation of Mount Melbourne tephra
890 compared with volcanic glasses of explosive eruption deposits produced by Mount

891 Rittmann (Di Roberto et al., 2019; Lee et al., 2019), The Pleiades (Lee et al., 2019),
892 Mount Melbourne (Lee et al., 2019), and Erebus volcano (Harpel et al., 2008). A-b)
893 Total alkali-silica diagram (TAS; LeBas et al., 1986), C) K₂O vs SiO₂ diagram, and D)
894 CaO vs SiO₂ diagrams showing the glass composition of studied products from Mount
895 Melbourne. Error bars represented 2 standard deviations of replicated analyses of the
896 MPI-DING StHs6/80-G secondary standard glass run alongside the marine tephra
897 samples

898 Figure 7. Selected trace element compositions of studied samples and comparison with
899 bulk rock compositions from literature: MB-07 and MB-43 from Armienti et al. (1991);
900 SE 03 157, SE 04 158, MM 05-185, MM 05-229, MM 15-229 from Worner et al.
901 (1989).

902 Figure 8. Primitive mantle (PM) normalized spider diagram (McDonough and Sun,
903 1995) showing the trace element distribution of the studied samples.

904 Figure 9. Age and K/Ca (derived from neutron-produced ³⁹Ar_K/³⁷Ar_{Ca} ratio) profiles
905 from step-heating experiments of two aliquots of feldspar separate from sample
906 MELS1-3. Data were acquired by a single-collector noble gas mass spectrometer
907 (MAP215-50, orange spectra) and a multi-collector noble gas mass spectrometer
908 (ARGUS VI, green spectra). Box heights indicate the 2σ analytical uncertainty.

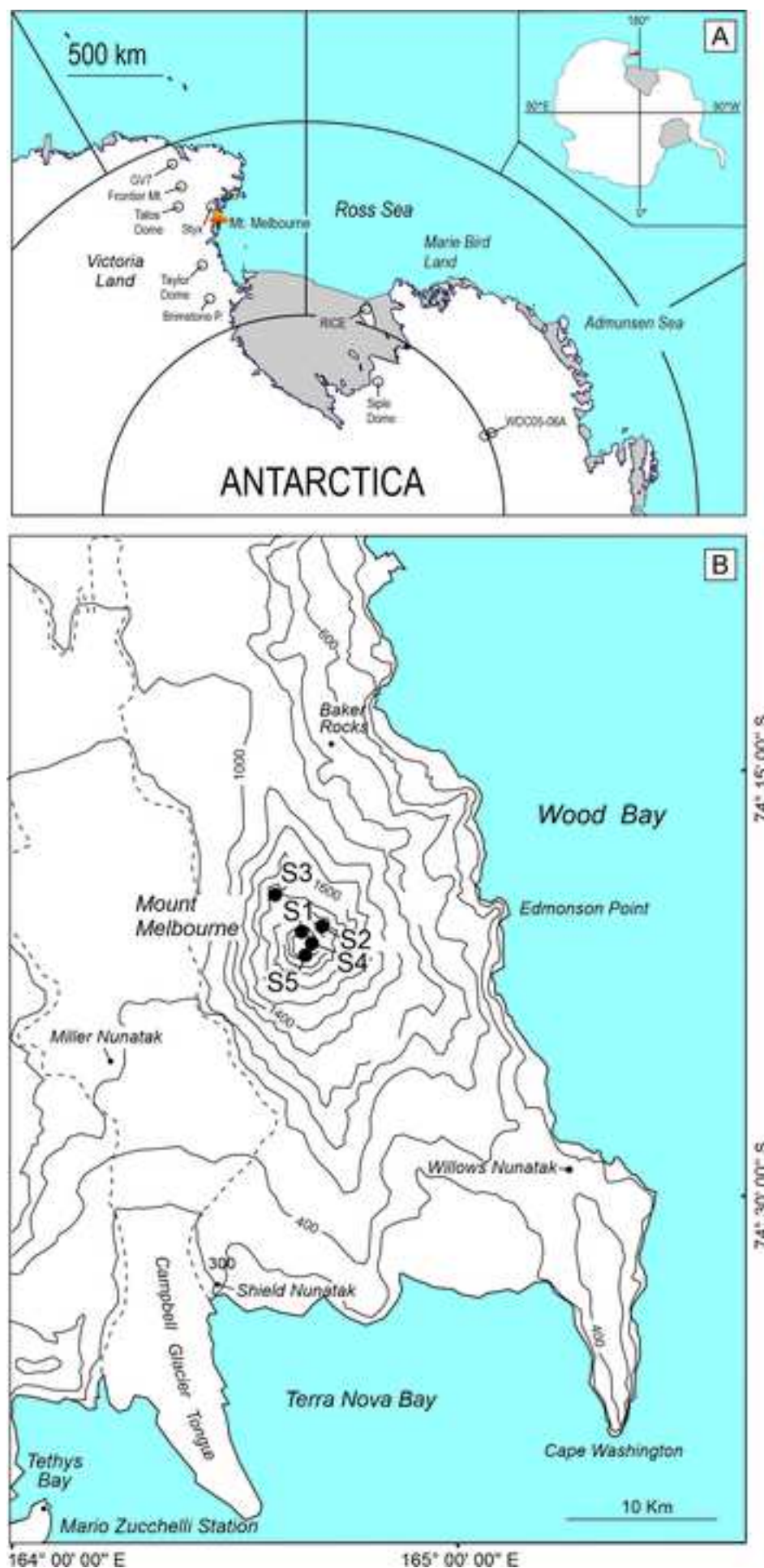
909 Figure 10. Map of the summit area of Mount Melbourne volcano modified after that
910 published by Worner and Viereck (1990), and integrated by field observations and
911 analysis of satellite images. The distribution of deposits of the studied eruptions is
912 reported along with the precise position of stratigraphic sections

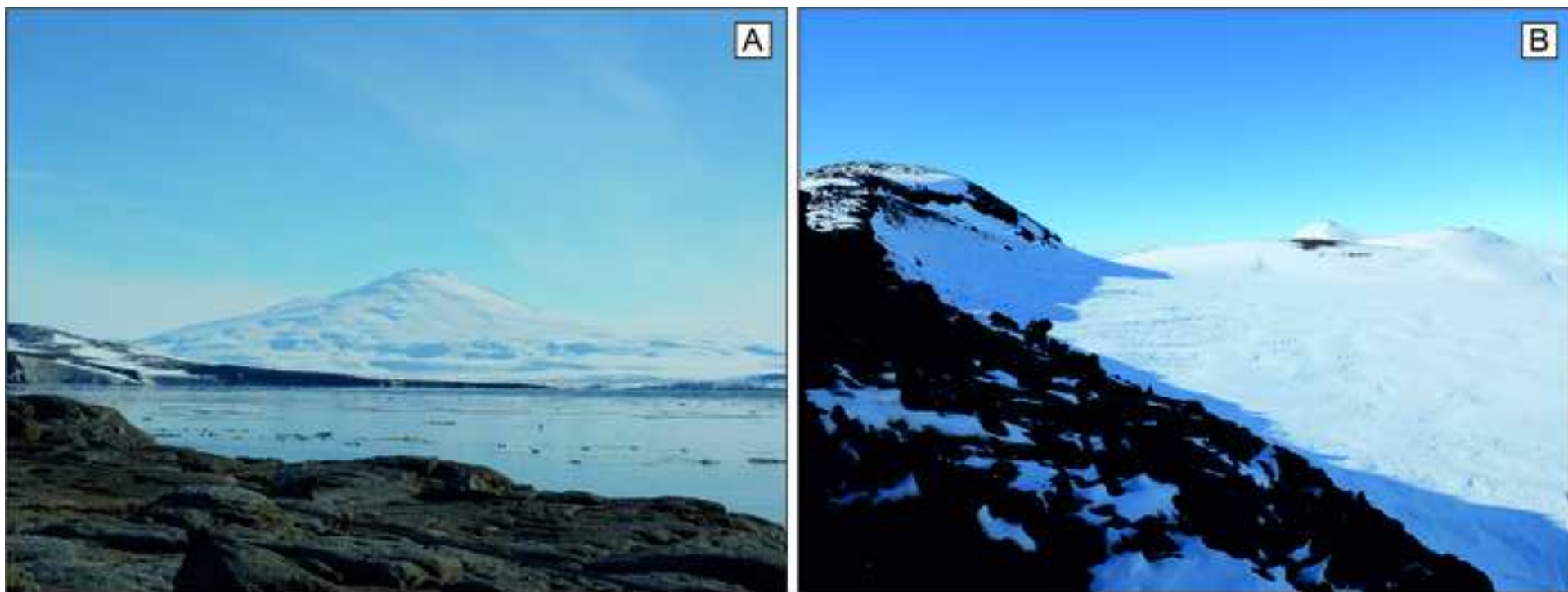
913

914 Supplemental Table 1. Major-element and trace-element data of single glass shards.

915 Supplemental Table 2. Full ⁴⁰Ar-³⁹Ar laser data on feldspar MELS1-3.

916 Supplemental Table 3. Composition of feldspar from MELS1-1 and MELS1-3
917 samples.





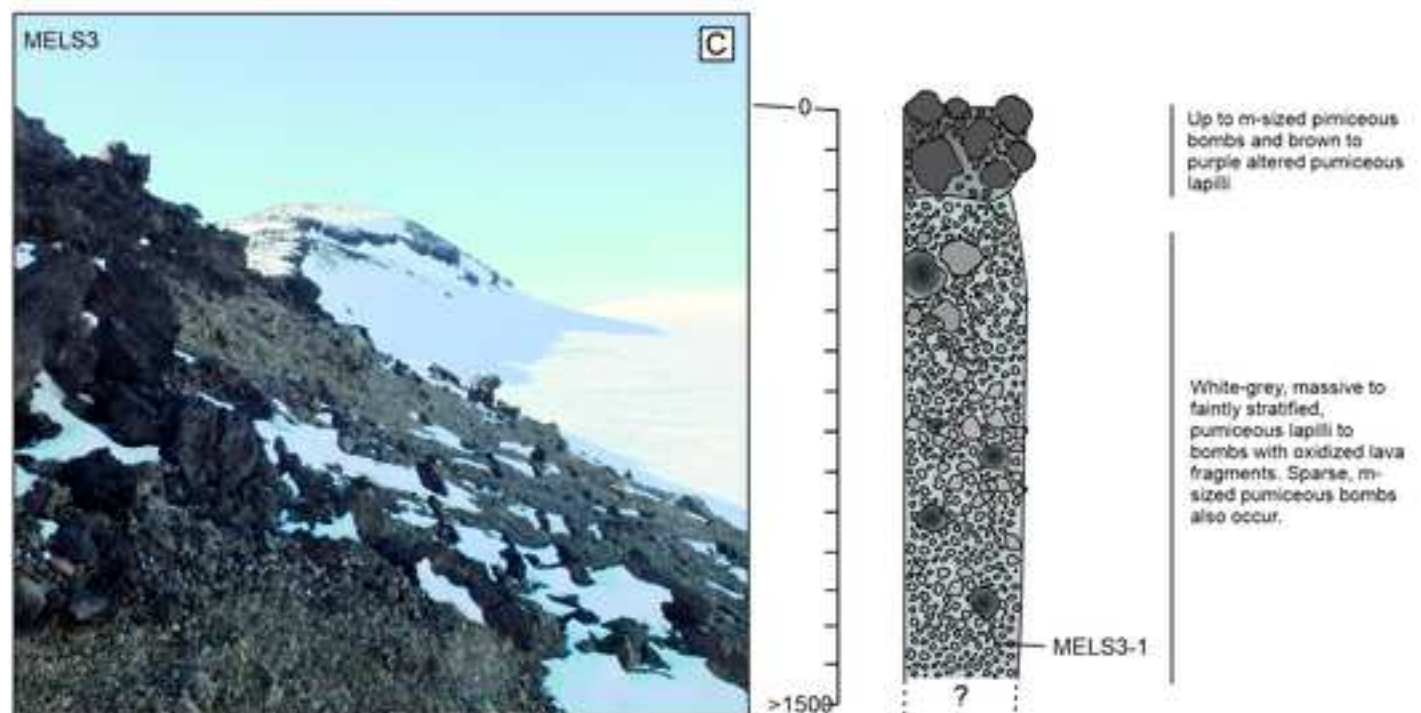
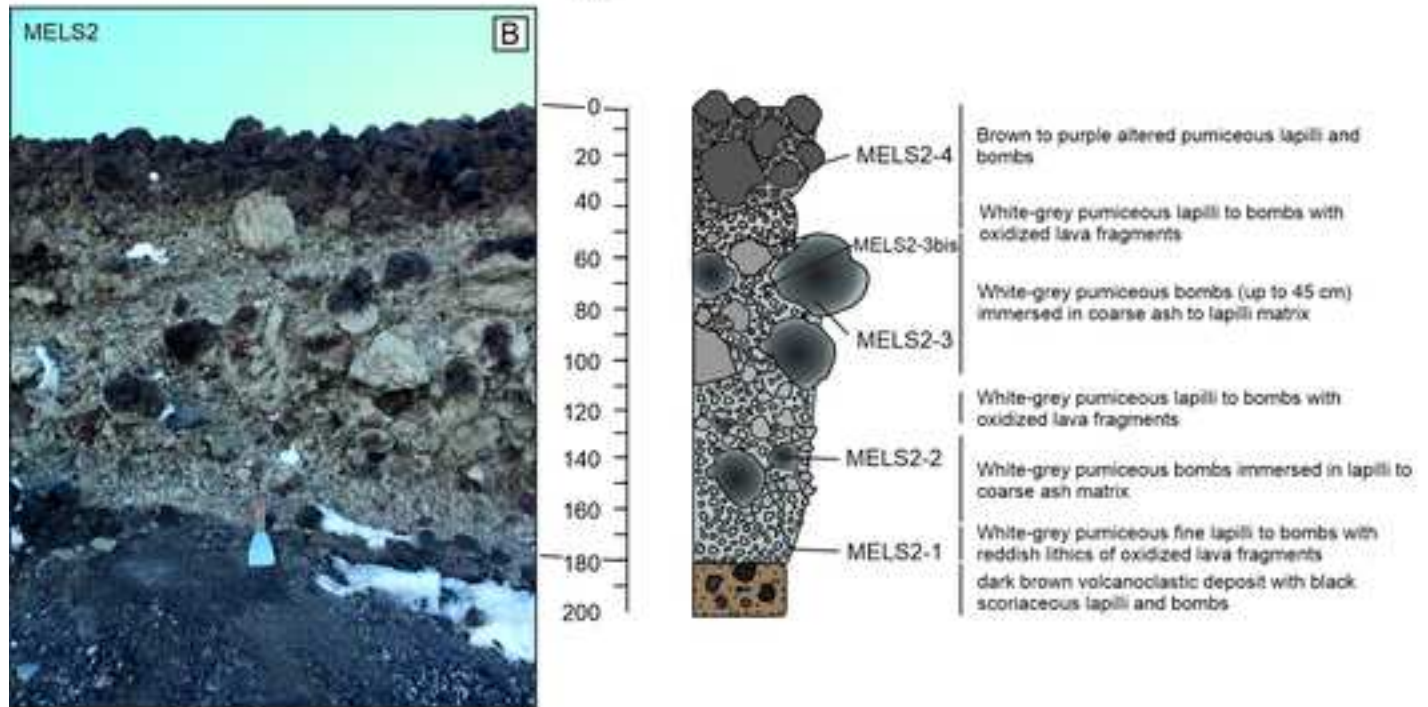
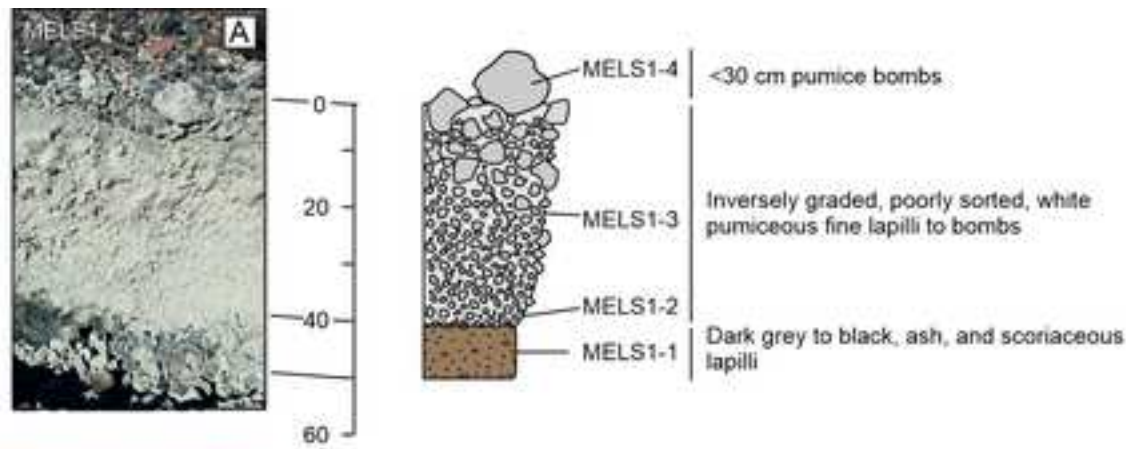
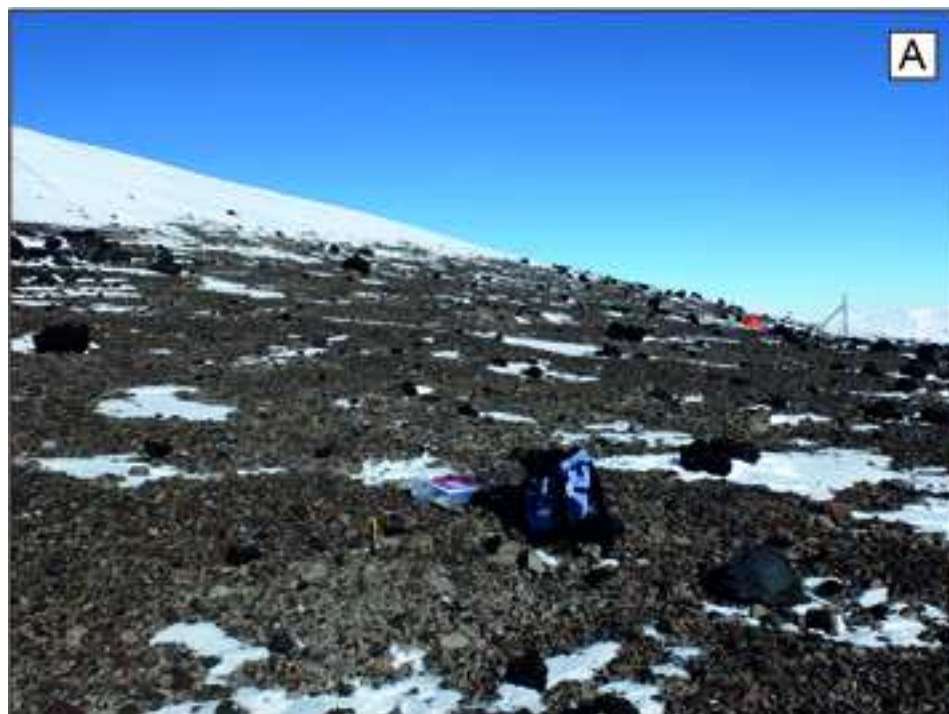


Figure 4

[Click here to access/download;Figure;Figure 4.jpg](#)



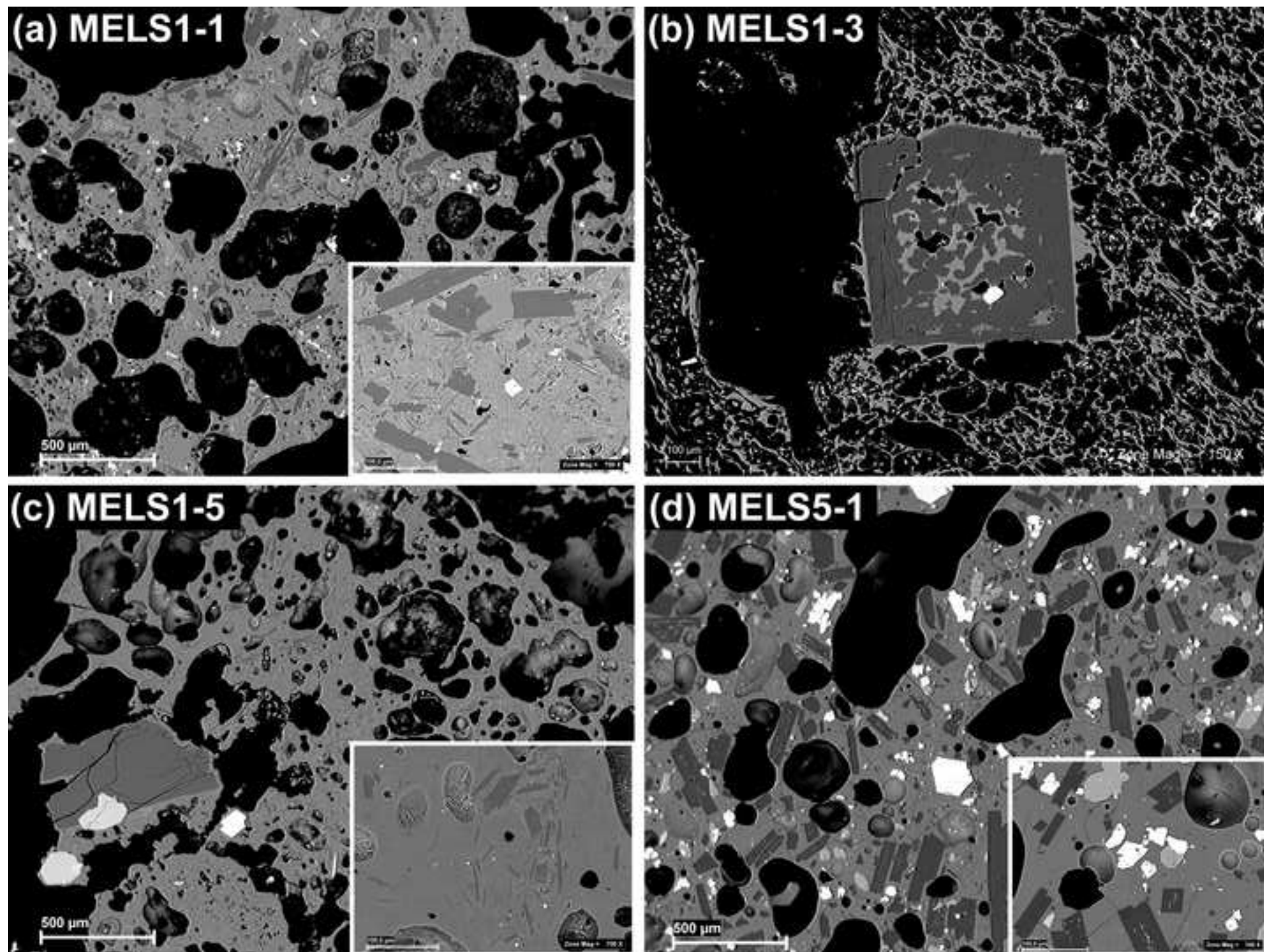


Figure 6

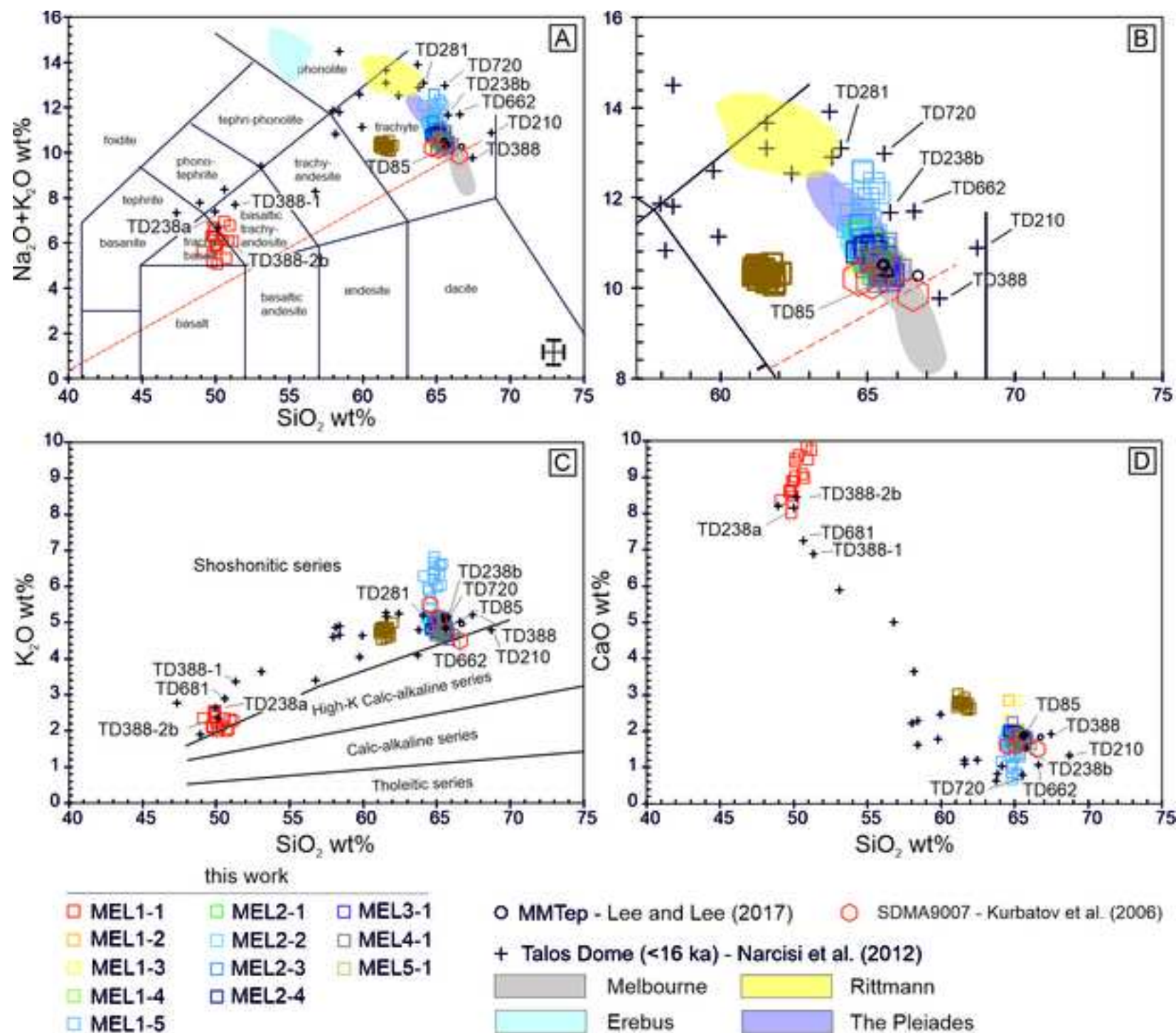
[Click here to access/download;Figure;Figure 6.jpg](#)

Figure 7

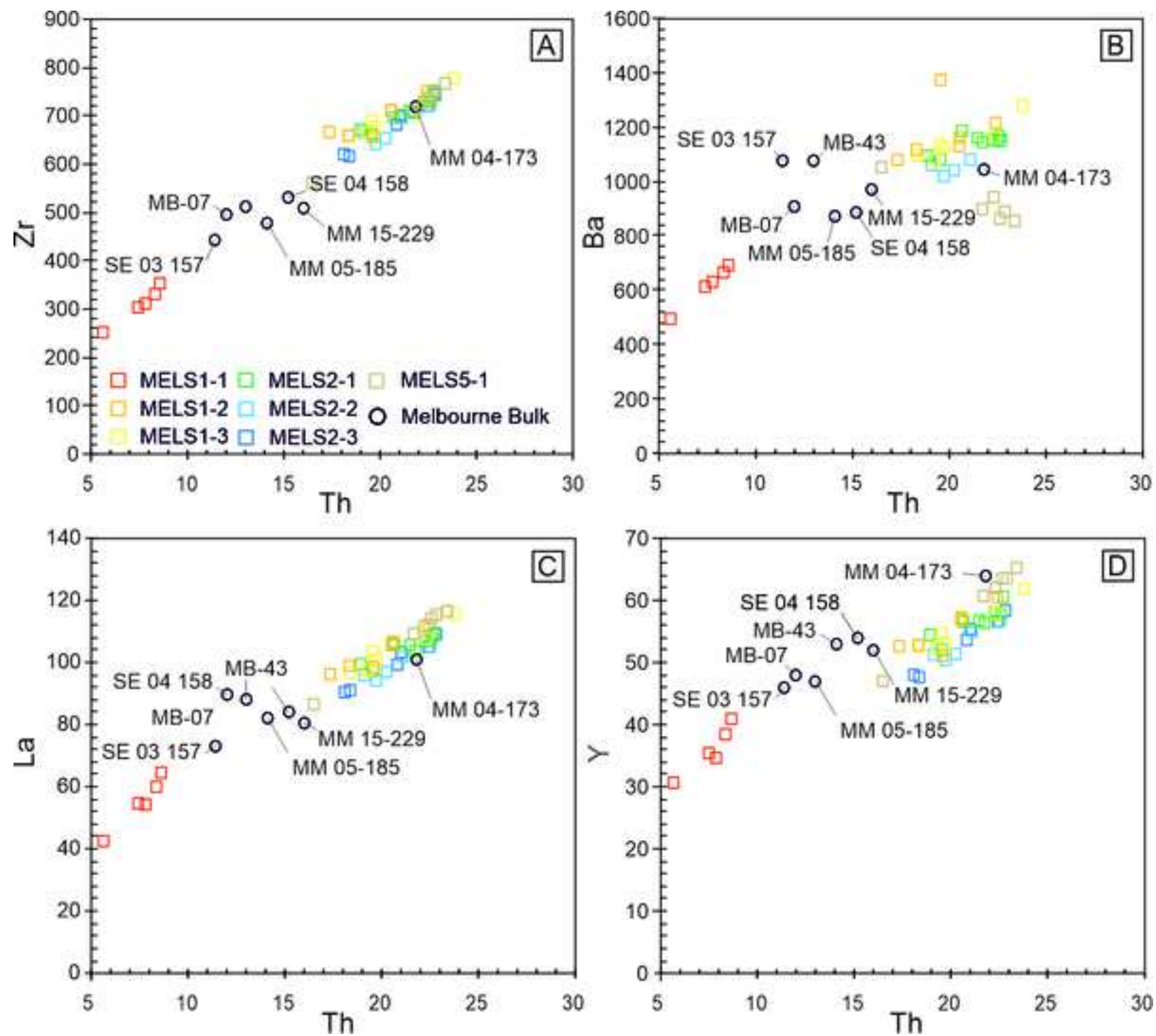
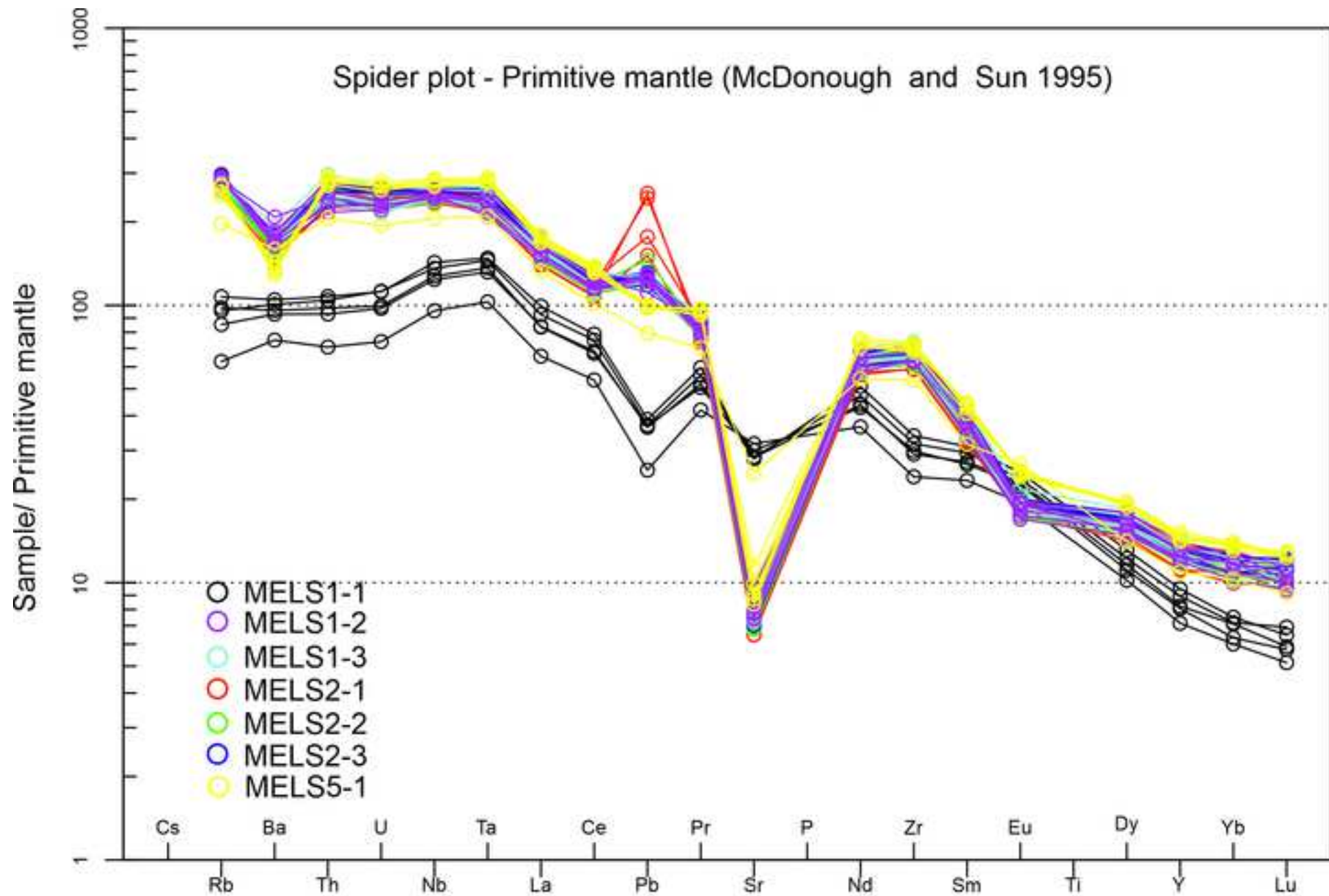


Figure 8

[Click here to access/download;Figure;Figure 8.jpg](#)

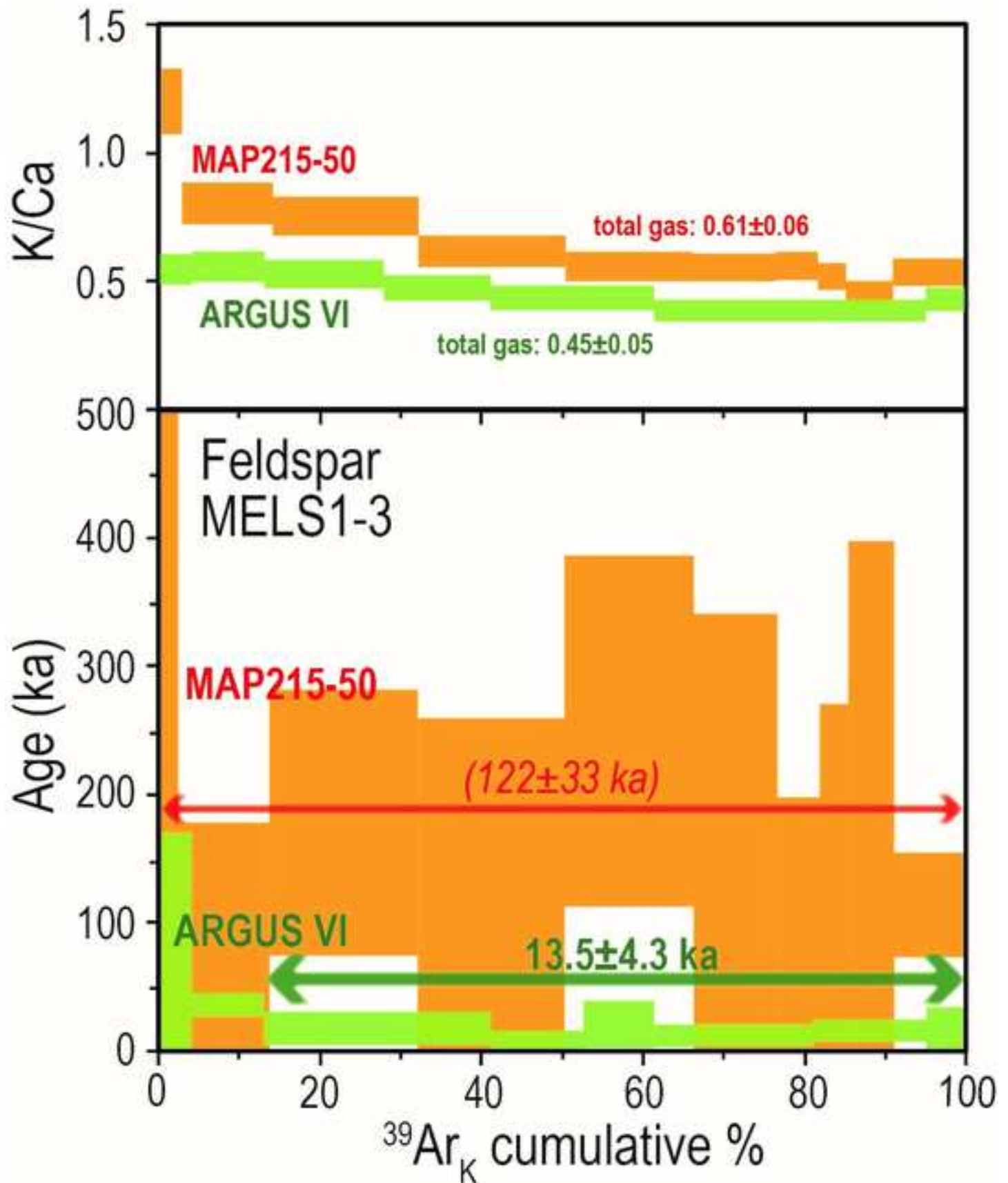


Figure 10

